RESEARCH ARTICLE

Does "right" simulated extreme rainfall result from the "right" representation of rain microphysics?

Huiqi Li[1] | **Yongjie Huang[2]** | **Yali Luo[3]** | **Hui Xiao[1]** | **Ming Xue[2,4]** |
Xiantong Liu[1] | **Lu Feng[1]**

[1]Institute of Tropical and Marine Meteorology/Guangdong Provincial Key Laboratory of Regional Numerical Weather Prediction, China Meteorological Administration, Guangzhou, China

[2]Center for Analysis and Prediction of Storms, University of Oklahoma, Norman, Oklahoma USA

[3]State Key Laboratory of Severe Weather, China Academy of Meteorological Sciences, Beijing, China

[4]School of Meteorology, University of Oklahoma, Norman, Oklahoma USA

Correspondence
 Yongjie Huang, Center for Analysis and Prediction of Storms, University of Oklahoma, Norman, OK, 73072, USA.
Email: huangynj@gmail.com, yongjie.huang@ou.edu

Yali Luo, State Key Laboratory of Severe Weather, China Academy of Meteorological Sciences, Beijing, 100081, China.
Email: ylluo@cma.gov.cn

Funding information
National Key Research and Development Program of China, Grant/Award Number: 2022YFC3003902; National Natural Science Foundation of China, Grant/Award Numbers: 42030610, 42275008, 41905047, U2242203; The Guangdong Basic and Applied Basic Research Foundation, Grant/Award Number: 2021A1515011415; The National Natural Science Foundation of China, Grant/Award Numbers: 42075086, 41975138

Abstract

Using the observations from the two-dimensional video disdrometer and polarimetric radar, a detailed process-based evaluation of five bulk microphysics schemes in the simulation of an extreme rainfall event over the mountainous coast of South China is performed. Most schemes reproduce one of the heavy rainfall areas, and the National Severe Storms Laboratory (NSSL) scheme successfully simulates both heavy rainfall areas in this event. However, our analysis reveals that even the NSSL simulation still cannot accurately represent the rain microphysics for this event. Observational analysis shows that abundant small- and medium-sized (1–4 mm) raindrops are the main contributors to the extreme rainfall. All the simulations tend to underpredict raindrops for diameter around 3 mm. The Lin, WSM6, and Morrison simulations agree better with the observed drop size distribution (DSD) for diameters between 1 and 2 mm for higher rain rates. The Thompson simulation shows a relatively narrow distribution with overpredicted small-sized (1–2 mm) raindrops. The NSSL simulation has a broad distribution with more large (>4 mm) raindrops probably related to its efficient rain self-collection process at the low levels, which is conducive to producing extreme rainfall. Proper rain evaporation rate is important in generating cold pools with favorable strength for the maintenance of a convective system in this event. Similar results are obtained in the simulations of two additional extreme rainfall cases, in which the NSSL simulation also overpredicts large raindrops while the Thompson simulation produces more small raindrops. This study indicates that more efforts are needed to improve the representation of rain self-collection/breakup, rain evaporation processes, and DSD for extreme rainfall over South China. It also highlights the importance in careful consideration of rain DSD in addition to radar reflectivity and surface precipitation when analyzing simulations of extreme rainfall in order to avoid "wrong" interpretation of "right" results.

KEYWORDS

extreme rainfall, microphysics schemes, rain drop size distribution, rain self-collection/breakup

1 | INTRODUCTION

The simulation of extreme precipitation remains a great challenge for numerical models, especially over regions with a diverse underlying surface, for example, the mountainous coastal cities. In numerical models, the parameterization of cloud microphysics coupled with model dynamics through latent heating, condensate weight and radiative transfer is important in quantitative precipitation forecasting (Randall *et al.*, 2018). Uncertainty in microphysics schemes is one of the major causes of model errors (Tao and Moncrieff, 2009). Yu *et al.* (2018) showed that microphysics scheme possessed even more uncertainty than the planetary boundary layer scheme in terms of precipitation forecast.

Bulk and bin micrsophysics parameterizations are two approaches in representing microphysical processes. Bulk microphysics parameterizes cloud and precipitation processes by assuming semi-empirical description of particle size distribution, for example, exponential or gamma distributions (e.g., Lin *et al.*, 1983; Thompson *et al.*, 2004; Milbrandt and Yau, 2005; Mansell *et al.*, 2010). Because of the computational efficiency of bulk schemes, they are more widely used in operational systems or research than bin microphysics. Single-moment bulk schemes typically predict the hydrometeor mixing ratios (e.g., Lin *et al.*, 1983; Kessler, 1995) and double-moment bulk schemes typically predict the number concentrations of all or some of the hydrometeors beyond the mixing ratios (e.g. Thompson *et al.*, 2004; Milbrandt and Yau, 2005). Many studies (e.g. Morrison and Grabowski, 2007; Morrison *et al.*, 2009; Dawson *et al.*, 2010; Igel *et al.*, 2015; Johnson *et al.*, 2016; L. Luo *et al.*, 2018; Qian *et al.*, 2018; Y. Luo *et al.*, 2008) show that double-moment bulk schemes usually outperform single-moment schemes in terms of the ability to more accurately simulate size sorting, raindrop breakup, self-collection, evaporation process, etc. However, some studies indicated single-moment schemes can produce precipitation closer to observations than double-moment schemes. For example, Huang *et al.* (2020) found that the Weather Research and Forecasting (WRF) single-moment six-class (WSM6) scheme performed better than the Thompson and Morrison schemes in the simulation of a record-breaking rainfall event over Guangzhou, China. Therefore, there are lots of uncertainties in microphysics schemes due to the lack of a benchmark model and limited knowledge of the underlying physics (Morrison *et al.*, 2020).

Evaluation of microphysics schemes using available observations is important in understanding biases in microphysics schemes, which can lay a foundation for further development of microphysics schemes and a rational choice of microphysics schemes when simulating different weather systems in different regions. Some field campaigns have been conducted to collect intensive observations to verify and improve microphysics schemes, for instance, the Mesoscale Alpine Program (MAP; Bougeault *et al.*, 2001), the Improvement of Microphysical Parameterization through Observational Verification Experiment (IMPROVE; Stoelinga *et al.*, 2003), the Olympic Mountains Experiment (OLYMPEX; Houze Jr. *et al.*, 2017), and the Southern China Monsoon Rainfall Experiment (SCMREX; Luo *et al.*, 2017). Many studies utilized these valuable observation data and other advanced instruments to evaluate microphysics schemes (e.g., Lin and Colle, 2009; Gao *et al.*, 2011, 2018; Suzuki *et al.*, 2011; Morrison *et al.*, 2012; Grasso *et al.*, 2014; Varble *et al.*, 2014; Barnes and Houze Jr., 2016; Naeger *et al.*, 2017, 2020; Furtado *et al.*, 2018; Conrick and Mass, 2019; Planche *et al.*, 2019; Tridon *et al.*, 2019; Wang *et al.*, 2020; Huang *et al.*, 2021). Lin and Colle (2009) used the in-situ microphysical observations from IMPROVE-2 to examine four bulk schemes in the WRF model. They showed that the rapid graupel fallout resulted in overprediction of surface precipitation along the Cascade windward slopes in some schemes. The schemes that generated more graupel than snow produced more precipitation over the Oregon Coast Range (Lin and Colle, 2009). Comparing with the observations from surface disdrometer and polarimetric radar, Morrison *et al.* (2012) demonstrated that the Morrison scheme (Morrison *et al.*, 2009) produced a too large mean raindrop size and a weaker precipitation rate when simulating a midlatitude squall line. Grasso *et al.* (2014) evaluated the WSM6 microphysics scheme by comparing synthetic Geostationary Operational Environmental Satellite-13 (GOES-13) imagery at 10.7 μm of simulated cloud fields with observed GOES-13 imagery, and found that excessive conversion from cloud water to graupel and accretion of ice by snow caused the lack of ice in the upper troposphere. Furtado *et al.* (2018) utilized the radar observations from the SCMREX and cloud and precipitation retrieved from satellites in the A-train constellation to investigate the sensitivity of simulating a heavy rainfall case over South China to cloud microphysics parameterizations. They found that rain drop size distribution (DSD) strongly influences biases that are mainly due to the rain and low-level clouds, whereas differences in the parameterization of ice crystal sedimentation strongly influence variations in the effects of high clouds. Planche *et al.* (2019) utilized multifrequency cloud radar observations to assess the performance of Morrison and Thompson microphysics schemes in the simulation of a squall line over Oklahoma. They revealed that the simulated DSD properties were closely related to the parameterization of the melting process in the Thompson scheme while they were strongly affected by the breakup process in the Morrison scheme.

Many observation instruments providing microphysical information, such as polarimetric radar and two-dimensional video disdrometer (2DVD), have been set up in South China in recent years. Some studies took advantage of these observations to evaluate the capability of different microphysics schemes to simulate weather systems over South China (Qian *et al.*, 2018; Wu *et al.*, 2021; Zhou *et al.*, 2022). Wu *et al.* (2021) evaluated three double-moment microphysics schemes in the simulation of the outer rainband of typhoon *Nida* (2016) with polarimetric radar observations. They showed that the Morrison and Thompson schemes overpredicted the mass-weighted raindrop diameters while the WRF double-moment 6-class (WDM6) scheme underpredicted the diameters and produced excessive concentrations of smaller raindrops due to overactive warm-rain processes. Zhou *et al.* (2022) found that in a merger-formation bow echo event, the Thompson scheme produced raindrop size bias and weaker cold pools because of inefficient raindrop breakup and rain evaporation. In general, it is likely that a "right" precipitation result may result from inaccurate representation of rain microphysics in the model. There are also some studies evaluating the performance of different microphysics schemes in simulating extreme rainfall over South China (e.g., Huang *et al.*, 2020; Dong and Li, 2023; Zhou *et al.*, 2023), but they seldom compared the simulated microphysical characteristics with the observations. Dong and Li (2023) used WSM6, WDM6, WRF single-moment 7-class (WSM7), and WRF double-moment 7-class (WDM7) schemes to simulate an extreme rainfall case with daily rainfall exceeding 1,000 mm along the South China coast in August 2018. Zhou *et al.* (2023) assessed the capability of the Milbrandt and Yau, Thompson, and Morrison schemes to reproduce the precipitation and radar reflectivity features during June 7–8, 2020. They both found that accretion of cloud water by rain was the major source of rain water. However, few studies focus on the simulation of extreme rainfall under weak synoptic lifting, which tends to cause severe disasters in South China (Luo *et al.*, 2016; Huang *et al.*, 2019a; Huang *et al.*, 2019b) and puzzles forecasters as well as model developers. During June 21–22, 2017, an extreme rainfall event (with a maximum one-hour precipitation of 165 mm and a 12-hour accumulated precipitation of 464.8 mm) occurred under weak synoptic lifting over the mountainous coast of South China (Figure 1a). The extreme rainfall was associated with a quasi-stationary convective system (Figure 2a) supported by a mesoscale convergence line. Li *et al.* (2021) showed that the WRF model with the National Severe Storms Laboratory (NSSL) microphysics scheme was able to reproduce the evolution of the convergence line, convective system, and precipitation pattern in this event

(Figure 1b). They found different roles of terrain, land–sea contrast and cold-pool outflows in the formation of the mesoscale convective system producing the heavy rainfall. They focused on the dynamic and thermodynamic mechanisms for this event, but have not examined the microphysical characteristics. The objectives of this paper are to evaluate different microphysics schemes in the simulation of such extreme rainfall using observations from the 2DVD along with polarimetric radar and to understand the causes of the different results from the microphysics schemes in depth, then providing a possible reference for numerical experiment design for future study.

This paper is organized as follows. The next section introduces the data and methods. Section 3 compares the simulations with different microphysics schemes to the observations. The closing section gives a summary and conclusions.

2 | DATA AND METHODS

2.1 | Observation data

Data from the S-band polarimetric radar at Yangjiang (crossed circle in Figure 1a) are used. The following quality control procedures have been conducted for the radar data: non-standard blockage mitigation, identification of ground clutter and biological scatters, and threshold checks for the cross-correlation coefficient and signal-to-noise ratio. The polarimetric radar can provide information about the particle size, shape, and orientation by measuring the differential reflectivity (Z_{DR}) and other polarimetric variables besides the conventional radar reflectivity (Z_H) and radial velocity. Z_{DR} is useful for determining the mean particle size of the radar volume. Larger raindrops are more oblate and have larger Z_{DR} values. Combining Z_H and Z_{DR} gives information about the DSD (Brandes *et al.*, 2004; Kumjian, 2013). For comparison with the simulation, the radar data were interpolated to a 1-km grid and 30 vertical levels at 500-m intervals.

In addition, the 2DVD (Schönhuber *et al.*, 1997) provides in-situ observations of rain DSDs. The 2DVD at Enping station (triangle in Figure 1a), which is located about 10 km away from the auto weather station recording the maximum rainfall during this event, is adopted in this study. The measurement area of the 2DVD is 10 cm × 10 cm. The diameter, fall velocity, and oblateness of the raindrop can be derived. The data from the 2DVD have been quality-controlled following Tokay *et al.* (2013), and have been divided into 41 bins with central diameters of 0.1–8.1 mm at 0.2-mm intervals to determine DSDs every minute.
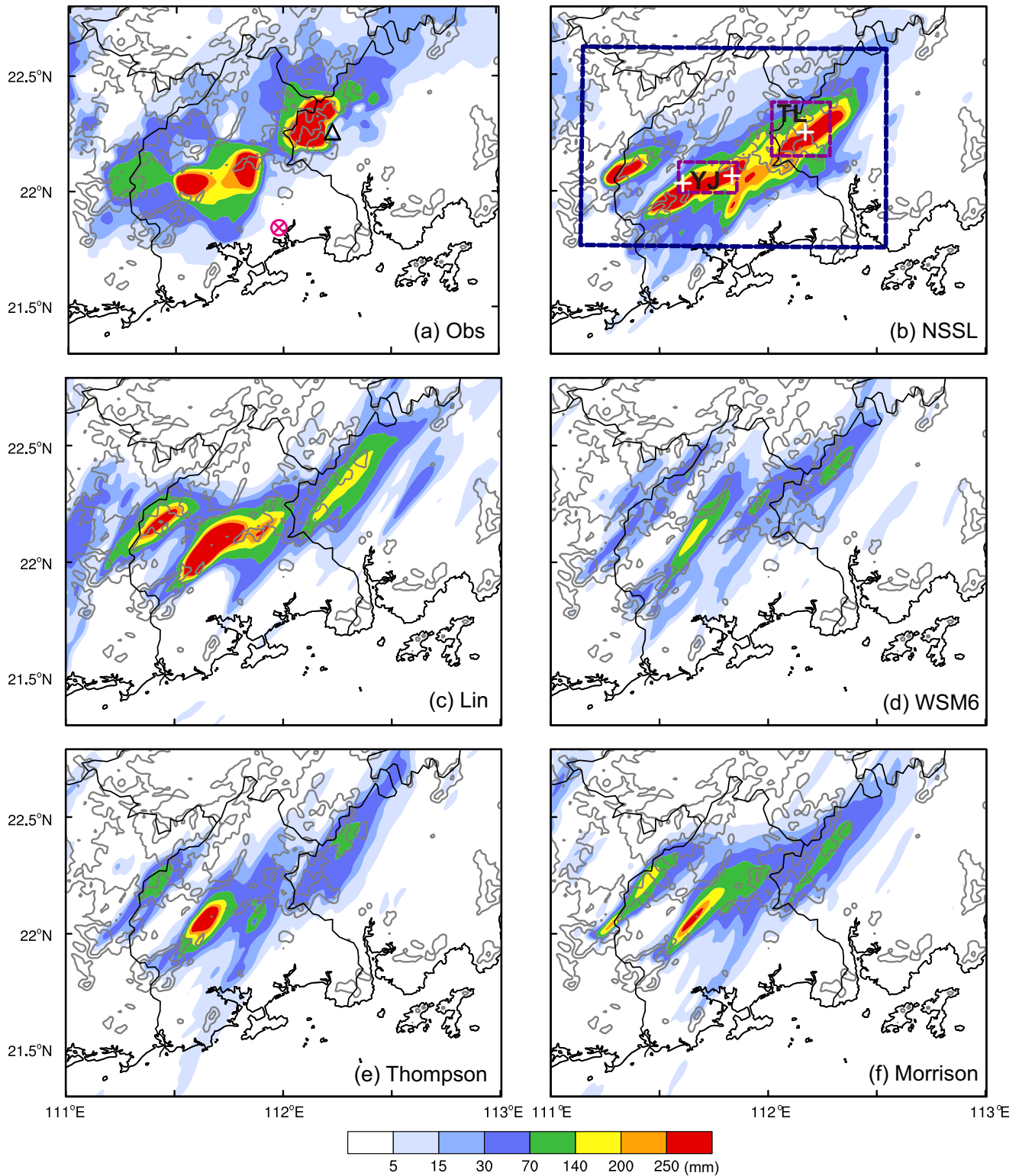
FIGURE 1 The 12-hour (1200 UTC June 21–0000 UTC June 22, 2017) accumulated rainfall (shaded, mm) for the (a) observation, and the simulations with the (b) NSSL, (c) Lin, (d) WSM6, (e) Thompson, and (f) Morrison schemes. The crossed circle and the triangle in (a) represent the locations of the Yangjiang radar and two-dimensional video disdrometer (2DVD), respectively. The blue rectangle in (b) indicates the main precipitation region in the present event. The purple rectangles in (b) denote the key areas (Yangjiang, abbreviated to YJ, and Mt. Tianlu, abbreviated to TL) of heavy rainfall mentioned in the text. Three plus marks indicate the locations of Tanshui, Gangmei, Jinjiang stations (from left to right). Terrain heights are contoured by gray lines at 200 and 500 m; similarly for the rest of the figures. [Colour figure can be viewed at wileyonlinelibrary.com]
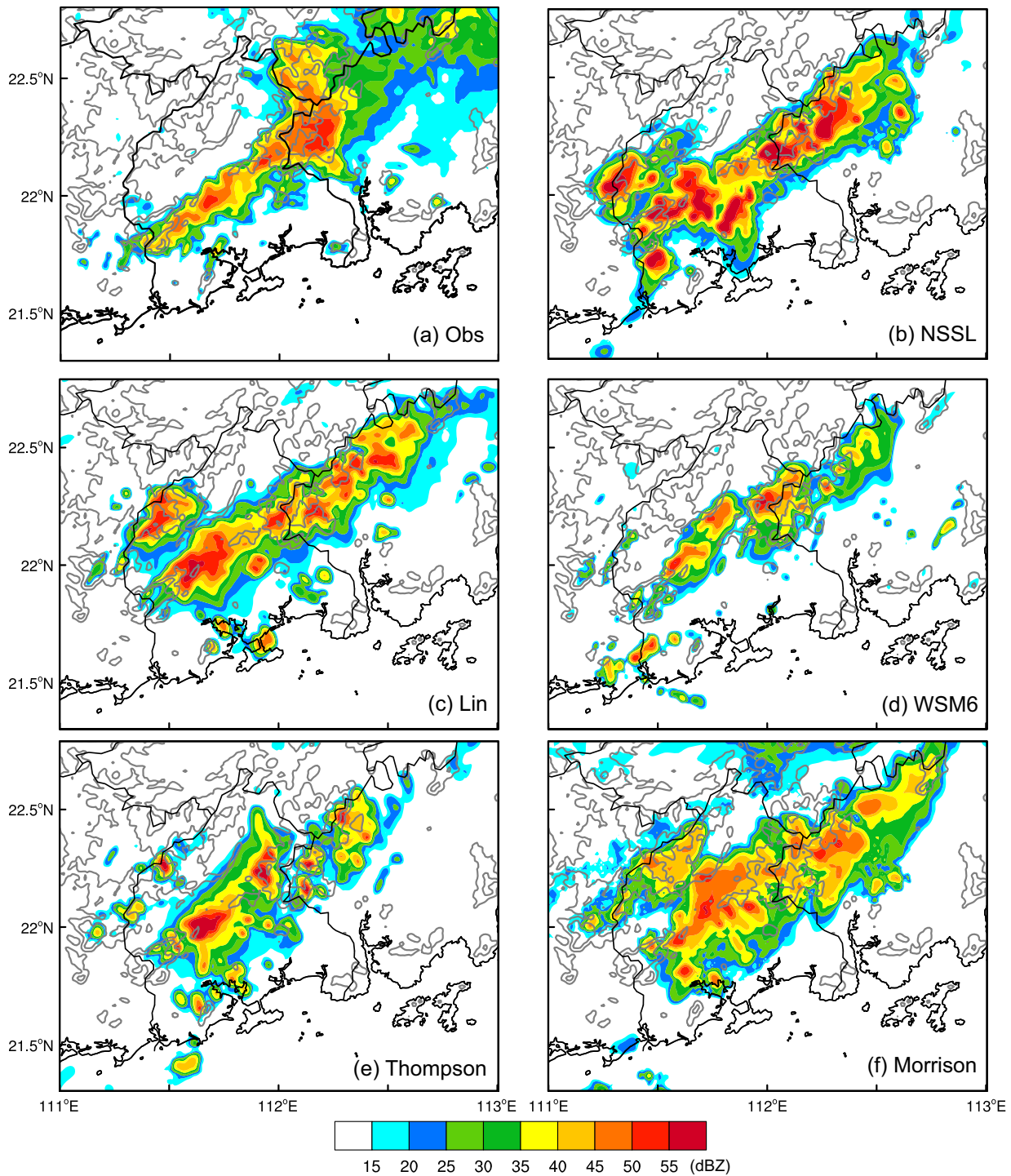
FIGURE 2 The composite radar reflectivity (dBZ) from the (a) observation at 1800 UTC June 21, 2017, and the simulations with the (b) NSSL, (c) Lin, (d) WSM6, (e) Thompson, and (f) Morrison schemes at 1700 UTC June 21, 2017. [Colour figure can be viewed at wileyonlinelibrary.com]

2.2 | Model configurations

The model configurations in this study are identical to those in Li *et al.* (2021), except for applying different microphysics schemes. Version 3.9.1 of the WRF model (Skamarock *et al.*, 2008) was adopted. A 9/3/1-km

domain configuration was used with 50 vertical levels. The ERA-Interim dataset (Dee *et al.*, 2011) at a horizontal resolution of 0.75° provided the initial and boundary conditions. The outermost domain was integrated from 0000 UTC June 21 to 0000 UTC June 22, 2017, and the two inner domains were activated six hours later but

TABLE 1 Description of experimental design

Experiment	Description
NSSL	Using the NSSL scheme from the beginning of the simulation (0000 UTC June 21). The control simulation in Li *et al.* (2021)
Lin	As the NSSL simulation but using the Lin scheme
WSM6	As the NSSL simulation but using the WSM6 scheme
Thompson	As the NSSL simulation but using the Thompson scheme
Morrison	As the NSSL simulation but using the Morrison scheme
Replacement experiments	Running with the NSSL scheme first but the microphysics scheme was replaced by the Lin/WSM6/Thompson/Morrison scheme at 1700 UTC June 21
NSSL_B	As the NSSL simulation but with modified rain self-collection/breakup processes
Thompson_B	As the Thompson simulation but with modified rain self-collection/breakup processes

ended at the same time. The physics schemes including the Rapid Radiative Transfer Model for Global Climate Models (RRTMG) long-wave and short-wave radiation scheme (Iacono *et al.*, 2008), Yonsei University's planetary boundary layer (PBL) scheme (Hong *et al.*, 2006), and Rapid Update Cycle (RUC) land surface scheme (Benjamin *et al.*, 2004) were used. Only the outermost domain applied the Grell–Freitas cumulus scheme (Grell and Freitas, 2014). Five microphysics schemes including the NSSL scheme (Mansell *et al.*, 2010), the Lin scheme (Lin *et al.*, 1983), the WSM6 scheme (Hong and Lim, 2006), the Thompson scheme (Thompson *et al.*, 2008) and the graupel-like Morrison (Morrison *et al.*, 2009) scheme were tested. Outputs from the 1-km domain every 10 min are analyzed in the following sections.

After a period of integration, the environment including the mesoscale flows and the development of cold pools may become quite different among different experiments. To examine the microphysical processes in different microphysics schemes under a similar early environment, four additional experiments (collectively referred to as replacement experiments, Table 1) were designed, which were run with the NSSL scheme first and then the microphysics scheme was replaced by the Lin, WSM6, Morrison or Thompson scheme at 1700 UTC June 21, around the formation of the linear convective system.

To make an apple-to-apple comparison with the polarimetric observations, polarimetric radar variables were derived with the polarimetric radar data simulator developed by Jung *et al.* (2008, 2010).

3 | EVALUATION OF DIFFERENT MICROPHYSICS SCHEMES

There were two heavy rainfall areas in this event: the middle of Yangjiang and the east of Mt. Tianlu (Figure 1a). The focus of this study is the microphysical characteristics of intense hourly precipitation over the two areas. Jinjiang station to the east of Mt. Tianlu, Gangmei station and Tanshui station in the middle of Yangjiang observed their maximum hourly precipitation (165, 99, 111.4 mm) during 1800–1900, 1900–2000, 2000–2100 UTC June 21, respectively. These three hours are analyzed in detail and two key areas (purple rectangles in Figure 1b, referred to as YJ and TL, respectively) are selected to perform the statistical analysis.

3.1 | Precipitation

In terms of 12-hour (1200 UTC June 21–0000 UTC June 22, 2017) accumulated precipitation (Figure 1), the NSSL simulation can reproduce the observed heavy rainfall (exceeding 250 mm) over YJ and TL with a simulated maximum accumulated precipitation of about 676 and 418 mm, respectively, while the simulations with other microphysics schemes produce a heavy rainfall center with smaller coverage over YJ and underpredict the rainfall near TL with the simulated maximum accumulated precipitation less than 200 mm (Figure 1). This suggests that the precipitation near TL where the terrain is more complex has a greater uncertainty related to microphysics than the precipitation over YJ. The NSSL, Lin, and Morrison simulations overpredict the maximum accumulated rainfall in the northwest of YJ by more than 70%. The evolution of reflectivity shows that all the schemes are able to simulate the convective initiation near the mountains, the convergence line and the linear convective system as observed, although the simulated linear convective system is not formed at exactly the same time as the observation (Figure 2). The NSSL simulation produces more intense storms with higher reflectivity (>55 dBZ, Figure 2b). The convective system in the Thompson simulation is less connected at that time (Figure 2e). In the WSM6 simulation, few convective cells are initiated near the coastal hill by 1700 UTC June 21 and the convective band is narrower (Figure 2d). The simulated convective storms near TL do not maintain over there as long as those in the observation, and instead they move northeast quickly and weaken, especially in the WSM6 and Thompson simulations, which

accounts for weaker rainfall near TL in these simulations (Figure 1).

3.2 | Rain drop size distribution

Figure 3 shows the distribution of rain rate $R(D)$ calculated with the 2DVD observations at Enping station and simulations during the peak rainfall hour and during the 12-hour period following Equation 1,

$$R(D) = \frac{\pi}{6} D^3 v(D) N(D), \tag{1}$$

where D is the diameter, N is the number concentration, and v is the terminal velocity in units of m·s^{-1} estimated using the empirical terminal velocity–diameter (v–D) relationship from Brandes *et al.* (2002), that is,

$$\begin{aligned} v(D) = &-0.1021 + 4.932D - 0.9551D^2 \\ &+ 0.07934D^3 - 0.002352D^4. \end{aligned} \tag{2}$$

It should be noted that D in Equation 2 is in units of mm during the calculation. The distribution of rain rate as a function of D is presented in order to easily see the contribution of rain drops for different sizes to the rain rate.

All the microphysics schemes evaluated in this study assume the rain DSD follows an inverse-exponential size distribution:

$$N(D) = N_0 e^{-\lambda D}, \tag{3}$$

where N_0 and λ are intercept and slope parameters, respectively. The single-moment schemes (Lin and WSM6) adopt a constant N_0 of 8×10^6 m^{-4} while the N_0 can vary in the double-moment schemes (Thompson, Morrison, and NSSL). Using the rainwater mixing ratio, number concentration (only double-moment schemes), assumed DSD, and v–D relationship from the simulations, the simulated distribution of rain rate can be derived and compared with the observations. It should be mentioned that in order to fairly compare how the DSD affects the rainfall in both simulations and observations, the same v–D relationship (Equation 2) is utilized to calculate the distribution of rain rate. The difference between the terminal velocity calculated with the v–D relationship within each microphysics scheme and that calculated by Equation 2 is not considered here.

The distributions are divided into four categories based on the integral precipitation intensity R for $0.1\,\text{mm} \leq D \leq 8.1\,\text{mm}$ [i.e., $\int_{0.1\,\text{mm}}^{8.1\,\text{mm}} R(D)dD$]: (C1) $R \geq 100\,\text{mm·hr}^{-1}$; (C2) $50\,\text{mm·hr}^{-1} \leq R < 100\,\text{mm·hr}^{-1}$; (C3) $20\,\text{mm·hr}^{-1} \leq R < 50\,\text{mm·hr}^{-1}$; (C4) $0.1\,\text{mm·hr}^{-1} \leq R < 20\,\text{mm·hr}^{-1}$. In the observation (black lines in

Figure 3), for the highest rain rate (C1), small- and medium-sized (1–4 mm) drops are major contributors to the rainfall (accounting for ∼84% of the rainfall, Figure 3a–c, Table 2). More large drops (>4.5 mm) appear for the higher rain rate classes (C1, C2) (Figure 3a–f). For the lower rain rate class (C4), rainfall is mainly contributed by the medium-sized drops (2–3 mm, accounting for ∼58%) during the peak rainfall hour (Figure 3j), while the statistics of the 12-hour period show that the main contributors shift to the smaller drops (1–2 mm, accounting for ∼57%) (Figure 3l). During the peak rainfall hour, the contribution of the small-sized drops (<2 mm) is more significant for C3 (∼34%, Figure 3g) compared with that for C4 (∼19%, Figure 3j).

In the simulations, in terms of higher rain rates (C1 and C2, Figure 3a–f), all the simulations except for the NSSL simulation (red in Figure 3) present a smaller diameter of peak rain rate than the observation, but their rain rates at 1–2-mm diameters are close to the observation (black in Figure 3). The NSSL simulation is in better agreement with the observation at 3–4-mm diameters. Larger raindrops make an important contribution to the high rain rates in the NSSL simulation, which is particularly evident in the distribution with rain rate greater than 100 mm·hr^{-1} (raindrops with diameter >4 mm account for more than half of the rainfall). For C1 (Figure 3a–c), the Lin (green in Figure 3) and Morrison (purple in Figure 3) simulations better fit the observed DSD in the range of 1.5–2.1 mm, but still underestimate the medium-sized raindrops. The Thompson simulation (orange in Figure 3) has a relatively narrow distribution, and overestimates the small-sized raindrops (raindrops with diameter <2 mm account for ∼40% of rainfall). The DSD in the Lin (green in Figure 3) and WSM6 (blue in Figure 3) simulations are prone to overpredict small-sized (1–1.7 mm) raindrops and underpredict medium-sized (2.5–3.5 mm) raindrops at rain rates lower than 100 mm·hr^{-1} (C2–C4, Figure 3d–l). For the lower rain rate class (C4), the peaks of all simulations shift to smaller sizes (1.1–1.9 mm) compared with the observation (2.7 mm) during the intense hourly rainfall period (Figure 3j,k). The contribution from raindrops with 2–3-mm diameter to the rain rate is much smaller in the simulations (<34%) than that in the observation (∼58%). The maximum raindrop size over TL in the Morrison simulation (purple in Figure 3) is larger than in other simulations (Figure 3j).

Overall, the rain rate distribution of the NSSL simulation tends to be broader in the case of higher rain rates due to the smaller slope parameter. Rainwater mixing ratio and number concentration in the NSSL simulation are also examined and it is found that the grid points with a high rain rate usually have a large mixing ratio and a relatively
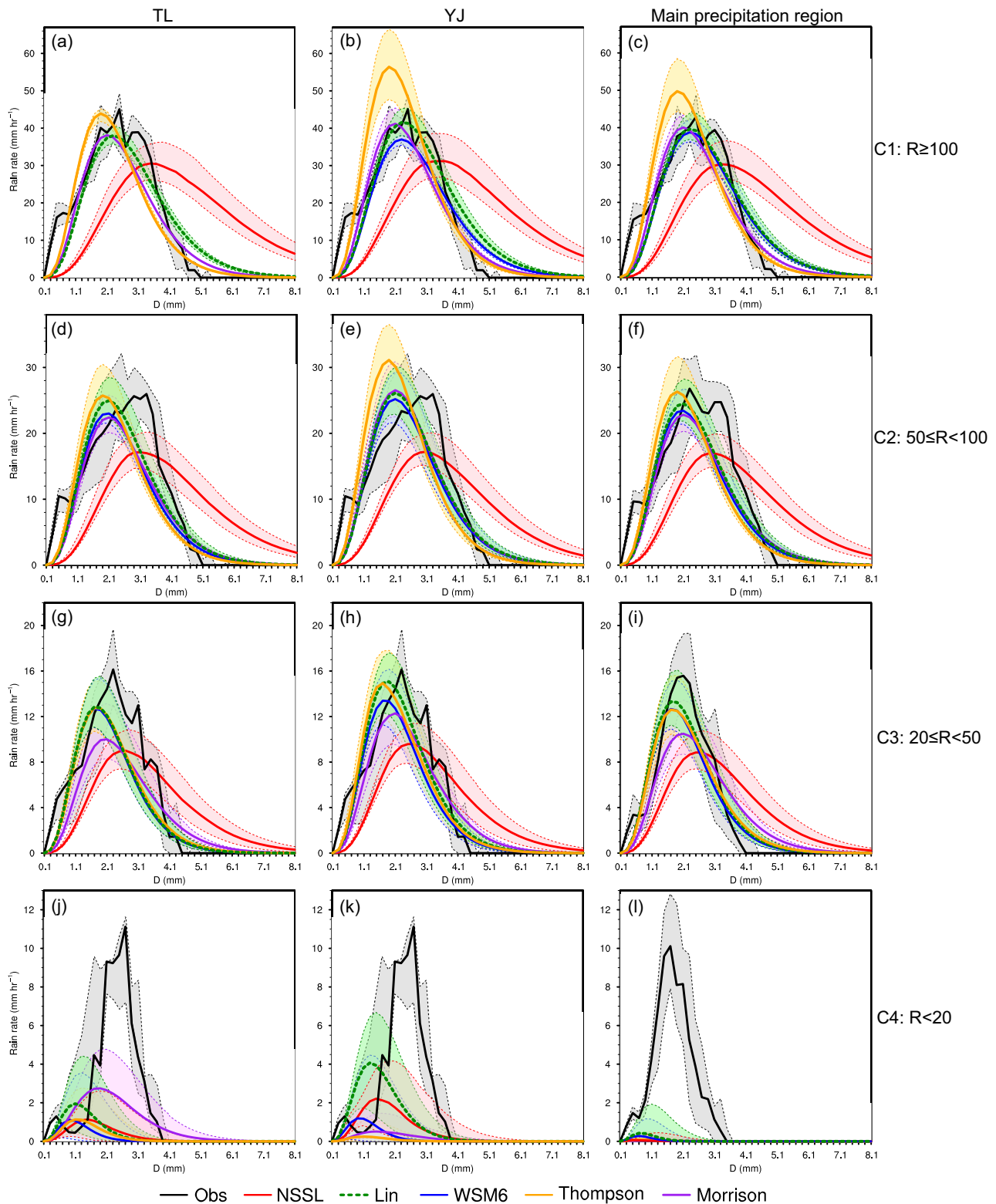
FIGURE 3 Observed and simulated distribution of rain rate [$R(D)dD$, where dD is the diameter bin size of 0.2 mm, the same as the two-dimensional video disdrometer [2DVD] observed) for the maximum hourly rainfall period over the key areas TL (left), YJ (middle), and during a 12-hour period over the main precipitation region (right). The black lines and associated gray shadings are identical in the left two columns, which represent the observations from the 2DVD during 1800–1900 UTC June 21, 2017. The distribution data are classified by the integral precipitation intensity: $R \geq 100$ mm·hr^{-1} (first row), 50 mm·hr$^{-1} \leq R < 100$ mm·hr^{-1} (second row), 20 mm·hr$^{-1} \leq R < 50$ mm·hr^{-1} (third row), 0.1 mm·hr$^{-1} \leq R < 20$ mm·hr^{-1} (fourth row). The thick lines represent the median values, and the shadings with thin dotted lines show the range between the 25th and 75th percentiles. Black: observation; red: NSSL simulation; green: Lin simulation; blue: WSM6 simulation; orange: Thompson simulation; purple: Morrison simulation.

TABLE 2 Contribution (%) of rain drops for different sizes (mm) to different integral precipitation intensity categories (C1: ≥ 100 mm·hr^{-1}; C2: 50 mm·hr^{-1} $\leq R <$ 100 mm·hr^{-1}; C3: 20 mm·hr^{-1} $\leq R <$ 50 mm·hr^{-1}; C4: 0.1 mm·hr^{-1} $\leq R <$ 20 mm·hr^{-1}) during the peak rainfall hour observed by the two-dimensional video disdrometer. Here the results are shown based on the median of drop size distributions

	$D < 1$ mm	1 mm $\leq D < 2$ mm	2 mm $\leq D < 3$ mm	3 mm $\leq D < 4$ mm	$D \geq 4$ mm
C1	10	23	35	26	6
C2	9	23	31	27	8
C3	9	25	41	21	3
C4	4	15	58	16	0

small number concentration (not shown), indicating the existence of large raindrops.

To explore the microphysical structure of the precipitation systems over the two key areas, the contoured frequency by altitude diagrams (CFADs; Yuter & Houze, 1995) of the observed Z_H and Z_{DR} and the corresponding cumulative CFADs during 1800–1900 and 1900–2100 UTC June 21 derived from radar measurements are displayed in Figure 4. The CFAD bin sizes are 5 dBZ for Z_H and 0.25 dB for Z_{DR}. The radar observation shows that frequency maxima of Z_H and Z_{DR} values below 5 km are around 45 dBZ and 0.75 dB over both key areas. About 45% of the Z_H values are between 40 and 48 dBZ below 2.5 km (the range between 50% and 95% contours in Figure 4a,b). The precipitation systems over TL appear more intense with 30% (red shadings) of 45 dBZ Z_H exceeding 4 km while those over YJ have 30% of 45 dBZ up to ~3.5 km (Figure 4a,b). At the low level, ~45% of the Z_{DR} values are between 0.5 and 1.6 dB over TL, and between 0.75 and 1.5 dB over YJ (Figure 4c,d). The large Z_{DR} values can reach about 2.75 dB. CFADs of Z_H and Z_{DR} only over the convective areas (identified using the algorithm of Steiner et al., 1995) within the key areas are also examined (not shown), and the patterns are similar to those in Figure 4, suggesting that convective precipitation is dominant during the intense hourly rainfall period and the convective properties are similar over the two areas.

Figures 5 and 6 show the CFADs of Z_H and Z_{DR} during the maximum precipitation hour in each simulation. For the TL area (left columns in Figures 5 and 6), the NSSL simulation shows overpredicted low-level reflectivity (Figure 5a). The frequency maxima in the Thompson simulation concentrate around lower Z_H (20–35 dBZ) and Z_{DR} (1.25–2.5 dB) values at the low levels (Figures 5g and 6g), which suggests the dominance of smaller raindrops in the Thompson simulation and is consistent with the rain DSDs in Figure 3. The Morrison simulation has slightly lower Z_H

values below 5 km and higher Z_H values above (Figure 5i) than the observation. It has approximately 45% of the Z_H values between 36 and 45 dBZ below 2.5 km. It is also noticed that the Morrison simulation exhibits the feature of a bright band related to the melting of frozen particles near 5 km, which is not observed. Most Z_{DR} values in the Morrison simulation concentrate around 3 dB (Figure 6i), greater than the observation (~0.75 dB, Figure 4c). When it comes to the YJ area (right columns in Figures 5 and 6), the NSSL and Lin simulations are apt to overpredict the low-level reflectivity (Figure 5b,d), while the WSM6 show slightly higher probabilities (~15%) around 35–40 dBZ below 3.5 km (Figure 5f). The precipitation system in the NSSL simulation has high frequency around 50-dBZ Z_H up to 2.5 km (Figure 5b) and around 3.5–4.25-dB Z_{DR} (Figure 6b). The Morrison simulation produces high probabilities around 35 dBZ below 5 km, and almost constant upward (Figure 5j). Below 2.5 km, there are 95% (cumulative frequency) of Z_H values below 57 dBZ in NSSL, below 52 dBZ in Lin, below 46 dBZ in WSM6, below 48 dBZ in Thompson and Morrison simulations (right column in Figure 5), compared with below 48 dBZ in the observation (Figure 4b). In general, the overpredicted Z_H and Z_{DR} in the NSSL simulation indicate the existence of more large raindrops, in accordance with the above analysis of DSDs.

A joint probability density function (PDF) is produced in Z_H–Z_{DR} space for both observation and simulations (Figure 7). Every point in the diagram represents the total frequency in the pair of Z_H–Z_{DR} data bin normalized by the total sample size (the number of grids within the blue rectangle in Figure 1b and below 3 km during 1800–2100 UTC June 21). It shows a combination of Z_H and Z_{DR}, and indicates a DSD (Brown et al., 2016). The PDF of the observations is characterized by peak probabilities around 20–25 dBZ and 0–0.25 dB (Figure 7a).

The PDF of the simulated Z_H and Z_{DR} is shown in Figure 7b–f. The Lin and WSM6 simulations have similar PDFs (Figure 7c,d), which is also seen in Brown et al. (2016). The high frequency around 5–10 dBZ and 0 dB suggests the prevalence of small raindrops, consistent with the aforementioned analysis. The narrow distribution in the Lin and WSM6 simulations is because these schemes use a fixed intercept parameter and thus an increase in liquid water content directly leads to a decrease in the slope parameter. By contrast, the two free DSD parameters in the double-moment scheme allow for more variation of DSD, resulting in broader coverage of the Z_H–Z_{DR} phase space (Putnam et al., 2017). Peak frequency in the NSSL simulation is around 30–35 dBZ and 2.5 dB, and the maximum Z_H and Z_{DR} values are greater than those in other simulations (Figure 7b). The PDF of the Thompson simulation looks more similar to the observation despite high frequency around higher Z_{DR}
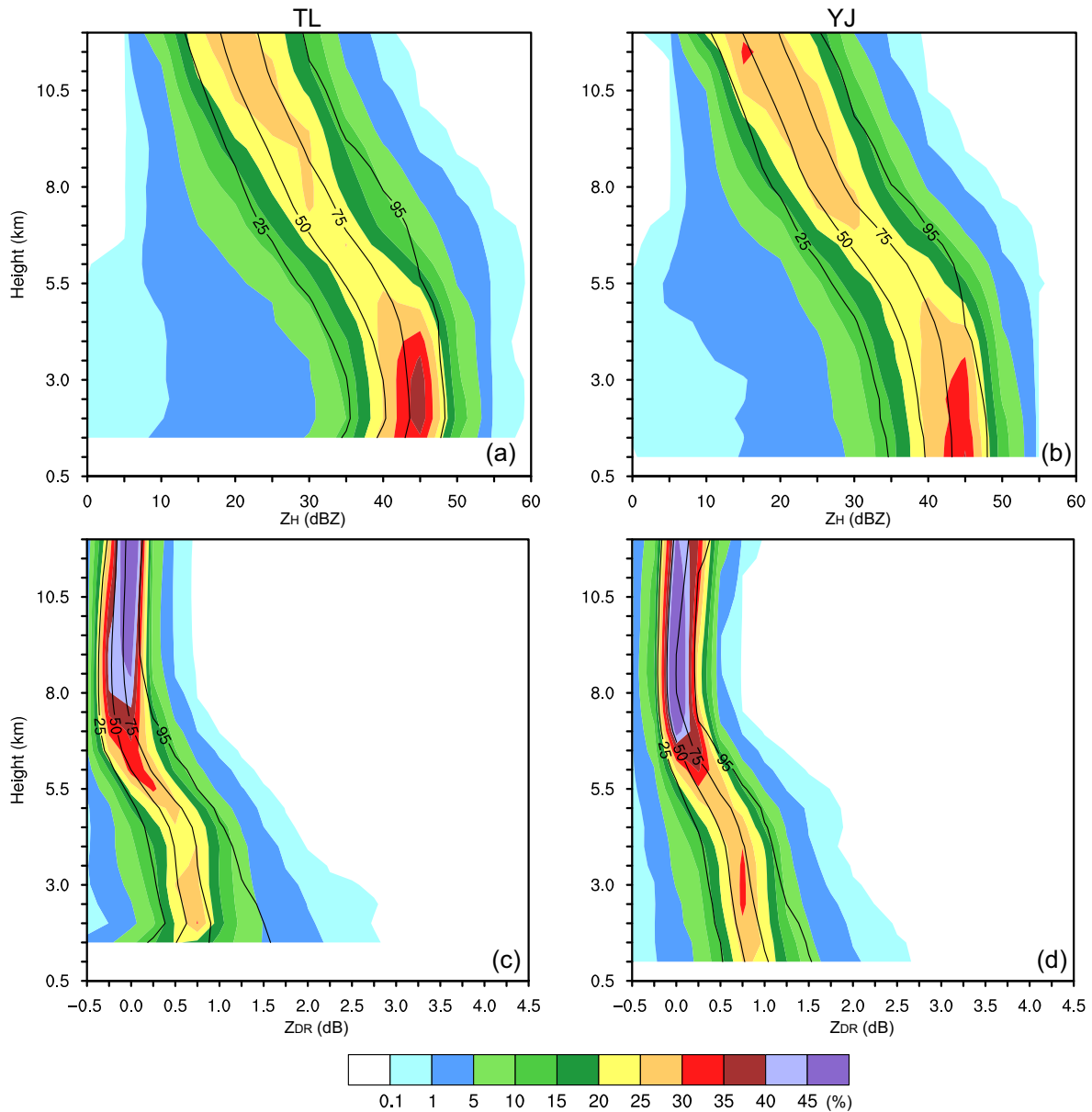
FIGURE 4 The contoured frequency by altitude diagrams (CFADs, shaded) of the observed (a, b) reflectivity (Z_H) and (c,d) differential reflectivity (Z_{DR}), and the corresponding cumulative CFADs (black contours) over the key areas TL (left) and YJ (right) during the maximum hourly rainfall period. Black contours indicate the cumulative frequencies of 25%, 50%, 75%, and 95% respectively. [Colour figure can be viewed at wileyonlinelibrary.com]

values (1–1.5 dB) (Figure 7e). The Morrison simulation exhibits high frequency around high Z_H (35–40 dBZ) and Z_{DR} (~2.75 dB) (Figure 7f). The PDFs of the Morrison and NSSL simulations indicate that the raindrops are generally larger than those in the observation.

3.3 | Microphysical processes related to rain production

It is of interest to investigate which microphysical processes make a primary contribution to the characteristics

of DSDs in different microphysics schemes. The vertical profiles of the main processes related to rain production (Table 3) for the maximum precipitation hour averaged over the two key areas (left and middle columns in Figure 8) and for the 12-hour period over the main precipitation region (right column in Figure 8) are shown in Figure 8. For all the schemes, the dominant processes influencing rain mixing ratio below the freezing level are the collection of cloud water by rain (PRACW) and rain evaporation (PREVP). And the melting of graupel (PGMLR) is evident near the freezing level. The contribution from autoconversion of cloud droplets to rain
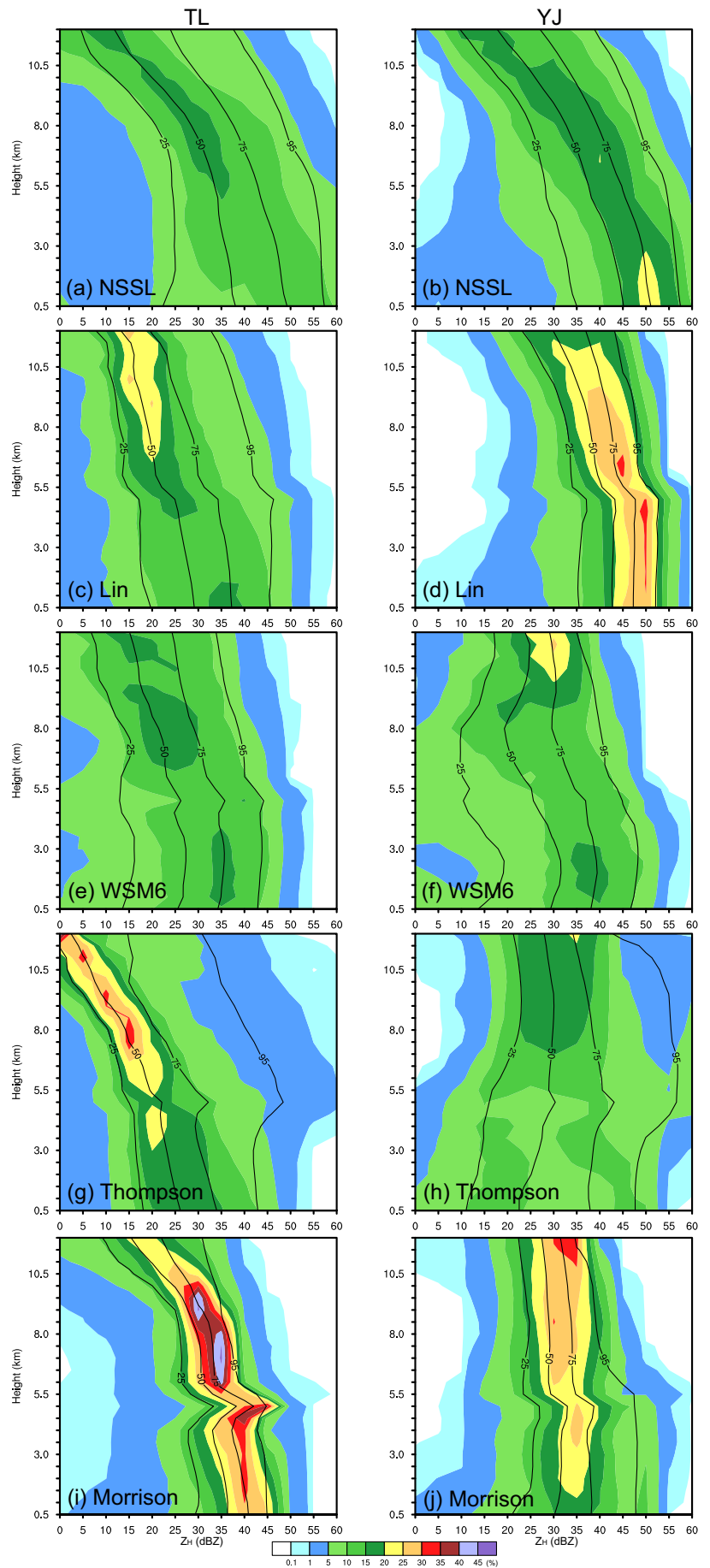
FIGURE 5 As in Figure 4a,b, but for the simulated Z_H for the (a,b) NSSL, (c,d) Lin, (e,f) WSM6, (g,h) Thompson, and (I,j) Morrison simulations. [Colour figure can be viewed at wileyonlinelibrary.com]
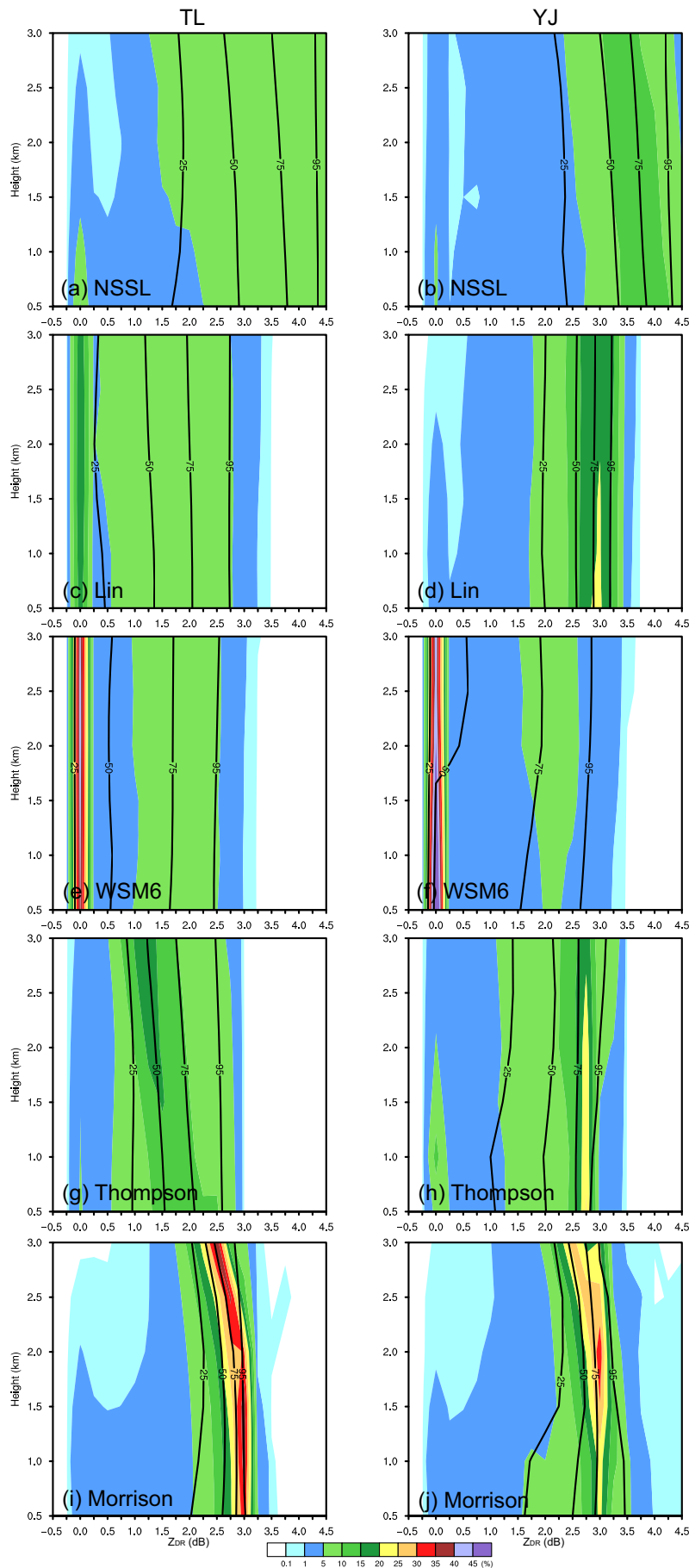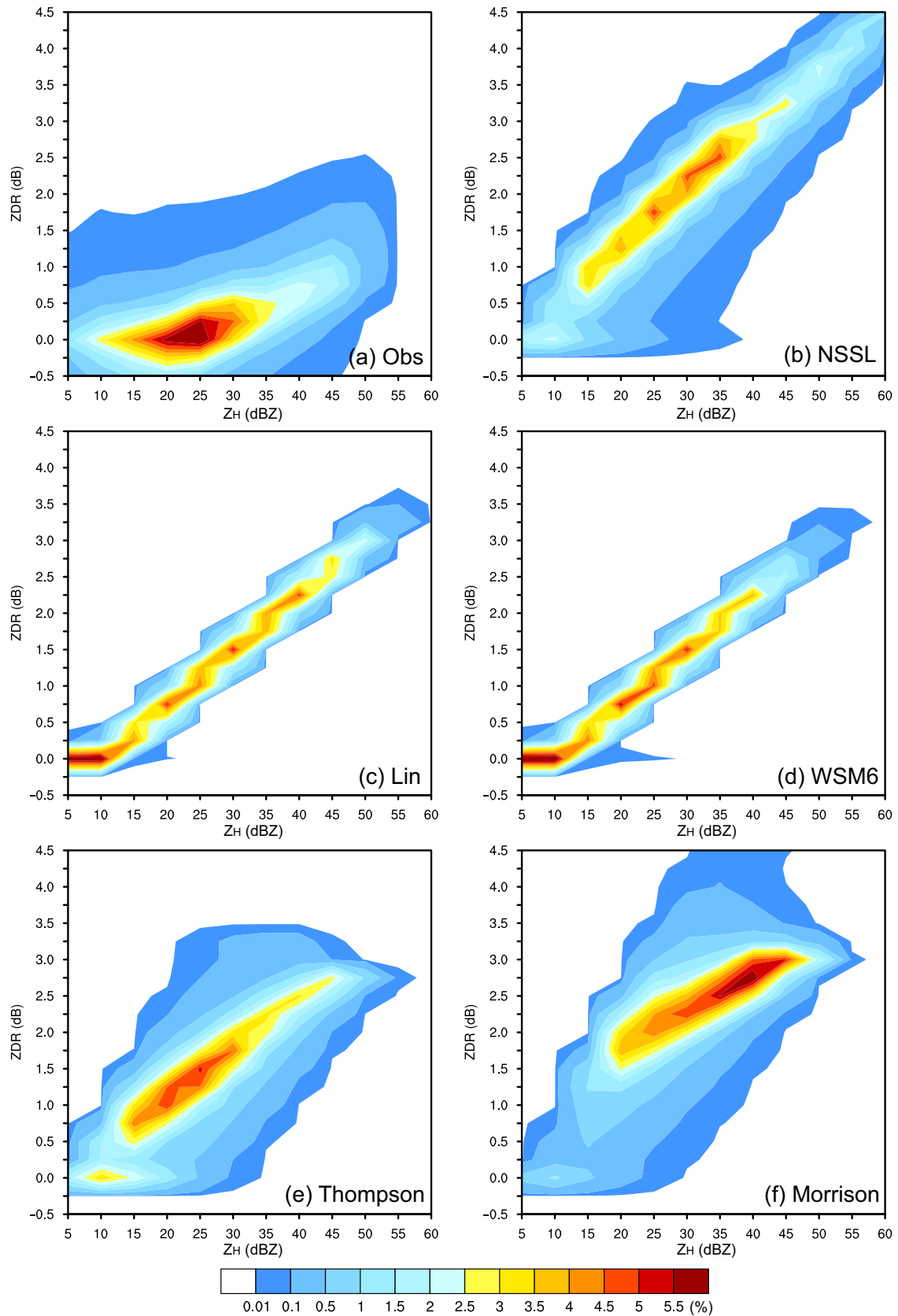
FIGURE 6 As in Figure 4c,d, but for the simulated Z_{DR} for the (a,b) NSSL, (c,d) Lin, (e,f) WSM6, (g,h) Thompson, and (I,j) Morrison simulations. [Colour figure can be viewed at wileyonlinelibrary.com]

FIGURE 7   The joint probability density function (PDF) of Z_H and Z_{DR} below 3 km over the main precipitation region: (a) observation, and simulations with the (b) NSSL, (c) Lin, (d) WSM6, (e) Thompson, and (f) Morrison schemes. [Colour figure can be viewed at wileyonlinelibrary.com]

TABLE 3 Description of the abbreviations for microphysical processes

	Abbreviation	Description
Changing rain mixing ratio	PRACW	Collection of cloud water by rain
	PRAUT	Autoconversion of cloud droplets to rain
	PREVP	Evaporation of rain
	PGMLR	Melting of graupel to rain
	PSMLR	Melting of snow to rain
	PGACR	Collection of rain by graupel
	PSACR	Collection of rain by snow
	PIACR	Collection of rain by ice
	PHMLR	Melting of hail to rain in the NSSL scheme
	PHACR	Collection of rain by hail in the NSSL scheme
	PGSHR	Shedding of graupel in the NSSL scheme
	PSSHR	Shedding of snow in the NSSL scheme
	PHSHR	Shedding of hail in the NSSL scheme
	PRSHR	Shedding of rain in the NSSL scheme
	PGEML	Enhanced melting of graupel by accretion of water in the WSM6 scheme
	PSEML	Enhanced melting of snow by accretion of water in the WSM6 scheme
Changing rain number concentration	NRAUT	Autoconversion of cloud droplets to rain
	NRACR	Self-collection/breakup of rain
	NREVP	Evaporation of rain
	NGMLR	Melting of graupel to rain
	NSMLR	Melting of snow to rain
	NGACR	Collection of rain by graupel
	NSACR	Collection of rain by snow
	NIACR	Collection of rain by ice
	NHMLR	Melting of hail to rain in the NSSL scheme
	NHACR	Collection of rain by hail in the NSSL scheme

mixing ratio is trivial and is just visible in the Lin and WSM6 simulations. The magnitude of the collection of cloud water by rain during the maximum hourly precipitation period is greater (with the maximum value of $\sim 2 \times 10^{-6}$ kg·kg^{-1}·s^{-1}) in the NSSL simulation over TL (Figure 8a), while it is greater (with the maximum value of $\sim 3 \times 10^{-6}$ kg·kg^{-1}·s^{-1}) in the Lin simulation over YJ (Figure 8e). For the 12-hour period over the main precipitation region, compared with other simulations (WSM6, Thompson, and Morrison), the NSSL and Lin simulations have a greater collection of cloud water by rain (Figure 8c,f), consistent with the stronger rainfall in these two simulations. The melting of graupel to rain in the melting layer is active particularly in the Lin simulation (Figure 8f). It implies that cold-phase processes, especially the melting of graupel, are of significance to the production

of rain in the Lin scheme, which is qualitatively consistent with the previous finding of Luo *et al.* (2010) in simulations of a heavy rainfall event along a Meiyu front over the Huai River basin in central East China. The melting of snow is generally smaller than the melting of graupel in all the simulations except for the Thompson simulation. On the other hand, the shedding processes are explicitly considered in the NSSL scheme. The magnitude of the shedding of graupel/hail is comparable to the accretion of rain by graupel/hail above the freezing level, and thus they almost offset each other (Figure 8a–c). In terms of the variation in rain number concentration in the double-moment schemes (Figure 9), rain self-collection/breakup (NRACR) causes noticeable reduction in the number concentration at the low levels in the NSSL simulation (Figure 9a–c). More active rain
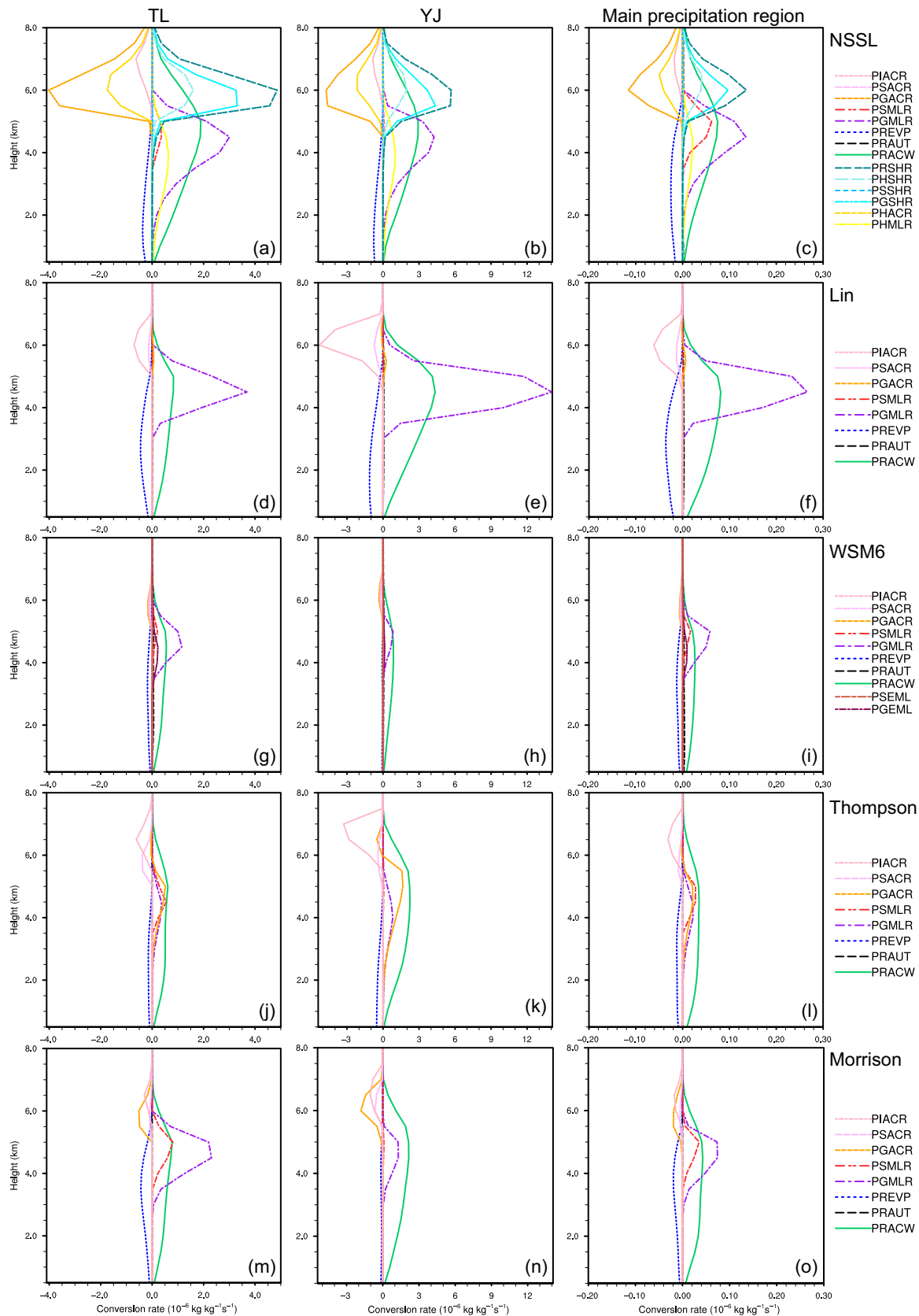
FIGURE 8 Vertical profiles of averaged mass conversion rates (10^{-6} kg·kg^{-1}·s^{-1}) related to rain production for the maximum hourly rainfall period over the key areas TL (left), YJ (middle), and during a 12-hour period over the main precipitation region (right) from the simulations with the (a–c) NSSL, (d–f) Lin, (g–i) WSM6, (j–l) Thompson, and (m–o) Morrison schemes. [Colour figure can be viewed at wileyonlinelibrary.com]
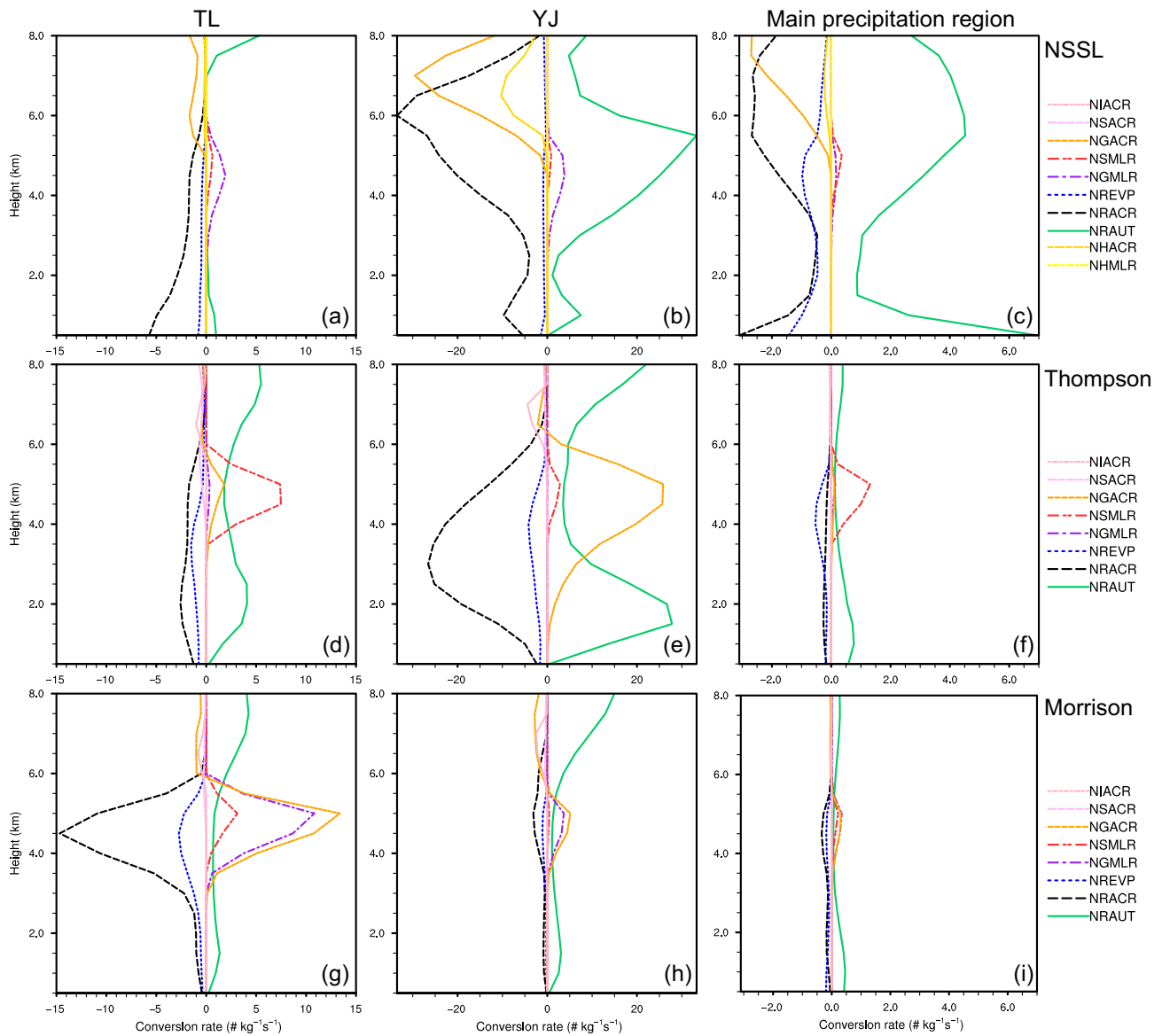
FIGURE 9 Vertical profiles of averaged number concentration tendency (kg^{-1}·s^{-1}) of rainwater for the maximum hourly rainfall period over the key areas TL (left), YJ (middle), and during a 12-hour period over the main precipitation region (right) from the simulations with the (a–c) NSSL, (d–f) Thompson, and (g–i) Morrison schemes. [Colour figure can be viewed at wileyonlinelibrary.com]

self-collection is beneficial to the growth of raindrops, and accounts for the shift to the large-diameter end in the low-level DSD of the NSSL simulation (Figure 3). The Thompson and Morrison simulations show large NRACR values at the higher levels (~2–3 km for Thompson, ~4.5–5 km for Morrison; Figure 9d,g). The autoconversion to rain (representing the collision and coalescence of cloud droplets) is the major source of the rain number concentration below the freezing level. The melting of graupel/snow is another source near 5 km above mean sea level in the three double-moment schemes while the collection of rain by graupel and then melting also make a notable contribution to the increase in rain number concentration in the Morrison scheme.

3.4 | Results from the replacement experiments

With the identical environmental conditions at 1700 UTC June 21 generated by the NSSL simulation, the results from the replacement experiments imply how the different microphysics schemes affect the simulation of the subsequent evolution of the convective system. Overall, the simulated precipitation near TL becomes stronger in these experiments (Figure 10) and is more similar to the observation compared with the corresponding experiments adopting the same microphysics scheme from the beginning of the simulation (Figure 1). Specifically, the simulated maximum 12-hour accumulated precipitation over TL is 341,
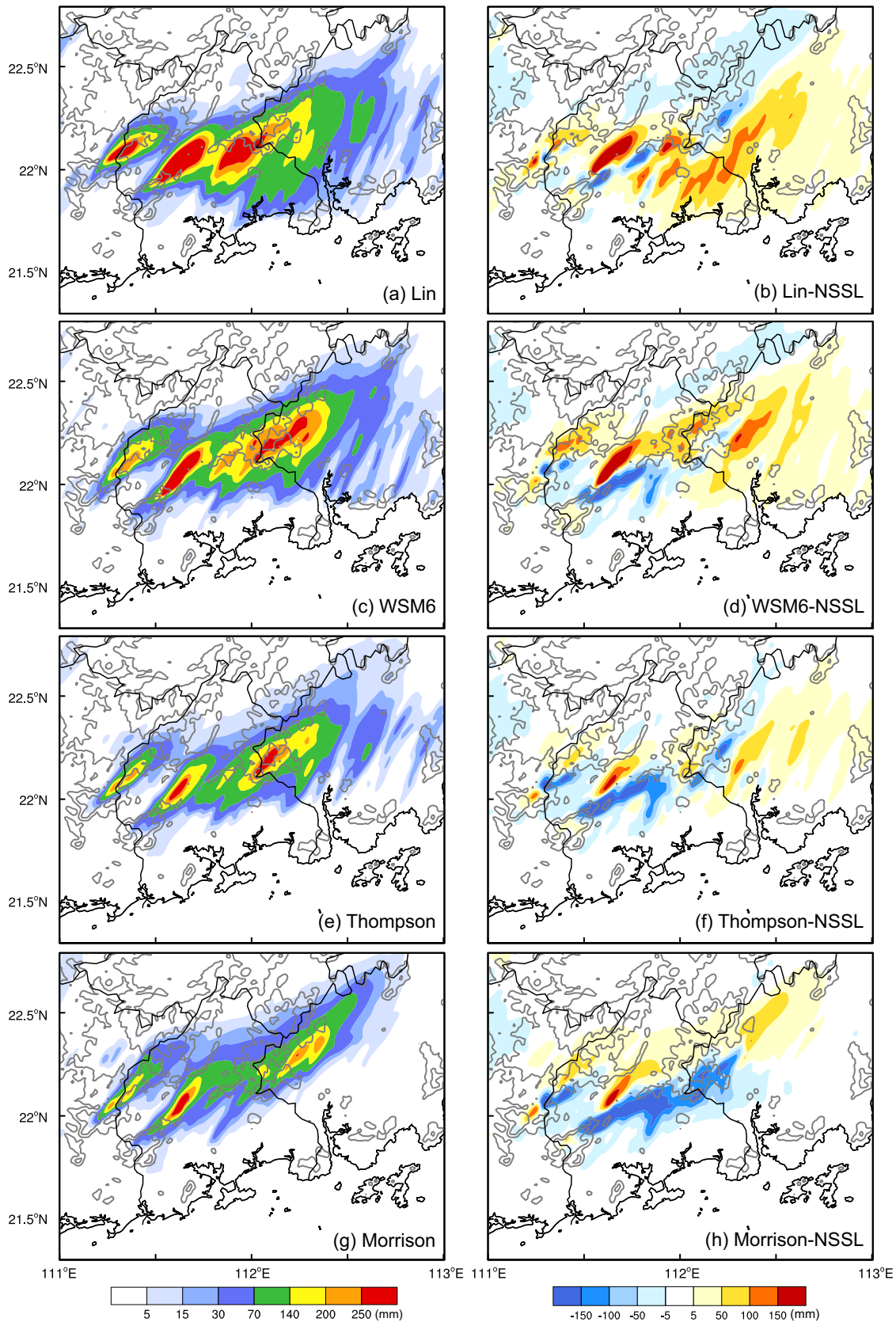
FIGURE 10   The seven-hour (1700–0000 UTC June 21–22, 2017) accumulated rainfall (left) for the replacement experiments with the Lin (first row), WSM6 (second row), Thompson (third row), and Morrison (fourth row) schemes, and the difference between these experiments and the NSSL simulation (right). [Colour figure can be viewed at wileyonlinelibrary.com]

390, 346, 332 mm in the Lin, WSM6, Thompson, Morrison replacement experiments, respectively, closer to the observed maximum value of 464.8 mm, compared with 197, 99, 84, 119 mm in their corresponding original experiments. The heavy rainfall centers in Yangjiang shift farther north in these experiments compared with the NSSL control simulation. It further demonstrates that the representations of microphysical processes in the microphysics schemes and their feedback to the thermodynamics fields have a significant impact on the simulated evolution of convection and associated rainfall even initialized with similar environmental conditions and initial development of convection. The simulated precipitation in the Lin replacement experiment covers a larger area to the southwest of TL (Figure 10a,b), which probably results from the fast spread of cold pools. Figure 11 displays the evolution of 300-K isotherms at 100 m above sea level which approximate the leading edges of cold pools. The Lin replacement simulation produces stronger cold pools while the NSSL simulation and the Morrison replacement simulation generate weaker cold pools that slowly spread southward. In the Lin replacement simulation, the stronger cold pools surge farther south, which was favorable for the development of convective storms farther south near the leading edge of cold pools with a back-building process, accounting for the larger coverage area of rainfall. This suggests that the thermodynamic fields quickly respond to different representations of microphysical processes in different microphysics schemes. The average vertical profiles of the budget terms for rain over the main precipitation region also show that the Lin replacement simulation has greater rain evaporation than other replacement simulations (Figure 12), giving rise to the stronger cold pools. In addition, the relative contributions from the main microphysical processes in the five schemes in Figure 12 are similar to those in Figure 8.

In addition, to further examine the microphysical processes in different microphysics schemes, identical instantaneous dynamic and thermodynamic fields were used to drive the five microphysics schemes to obtain the source and sink terms of rainwater. It should be noted that a large number of instantaneous fields (a total of 180 output fields with 352×292 horizontal grids in each output from the original NSSL, Thompson, and Morrison simulations) were used in order to provide different environmental conditions and ensure the robustness of the statistical results. The vertical profiles of averaged source and sink terms of rainwater mixing ratio and number concentration are presented in Figures 13 and 14, respectively. Only the grids with near-surface rain rate of 20 mm·hr^{-1} or higher are averaged because this study is more concerned with hourly heavy rainfall,

although the results using the threshold of 1 mm·hr^{-1} are similar. It is found that the NSSL scheme produces relatively smaller rain evaporation rate at the lower levels (Figure 13), because the rain DSD of the NSSL scheme extends to larger raindrops and given the same rain mixing ratio more larger raindrops will lead to a smaller evaporation rate (Dawson *et al.*, 2010; Gao *et al.*, 2011; Bryan and Morrison, 2012). The Morrison scheme has greater PRACW values above 2 km (with a maximum value around 11×10^{-6} kg·kg^{-1}·s^{-1}; Figure 13m). Consistently, the melting of graupel is prominent in the Lin scheme (Figure 13d–f). In other words, it seems difficult for the Lin scheme to produce the dominant role of warm-rain processes (at least in the present event), which is important in the formation of heavy rainfall during the pre-summer rainy season in South China (Yu *et al.*, 2022). Wu *et al.* (2022) also demonstrated that the double-moment schemes outperform the single-moment schemes in simulating the warm-rain processes in their experiments for a super typhoon. The large negative NRACR values are also noted at the low levels in the NSSL scheme (Figure 14). In a nutshell, the rain self-collection/breakup processes show distinctions among these microphysics schemes, and they play a vital role in determining the rain DSD.

3.5 | Sensitivity to the rain self-collection and breakup processes

In order to examine the impact of the rain self-collection and breakup processes on the simulated rain DSD, two sensitivity experiments based on the NSSL and Thompson schemes were conducted. These two schemes are further tested because they have relatively broader and narrower DSDs respectively, as illustrated above.

In the NSSL scheme, rain self-collection and breakup follow the method in Ziegler (1985),

$$\text{NRACR} = \begin{cases} E_c a_1 N_r^2 v_r^2 \frac{\mu+2}{\mu+1}, r_c < 50\ \mu m \\ E_c a_2 N_r^2 v_r, r_c \geq 50\ \mu m \end{cases}, \qquad (4)$$

where N_r is the rainwater number concentration, v_r is mean drop volume, μ is rain shape parameter, r_c is collector drop radius, and a_1, a_2 are the coefficients in the polynomial collection kernel for small drop and large drop, respectively. The breakup effect is represented by a breakup coalescence efficiency parameter E_c,

$$E_c = \begin{cases} 1, r_0 < 0.03\ \text{cm} \\ \exp[-50(r_0 - 0.03)], 0.03 \leq r_0 \leq 0.1\ \text{cm} \\ 0, r_0 \geq 0.1\ \text{cm} \end{cases}. \qquad (5)$$
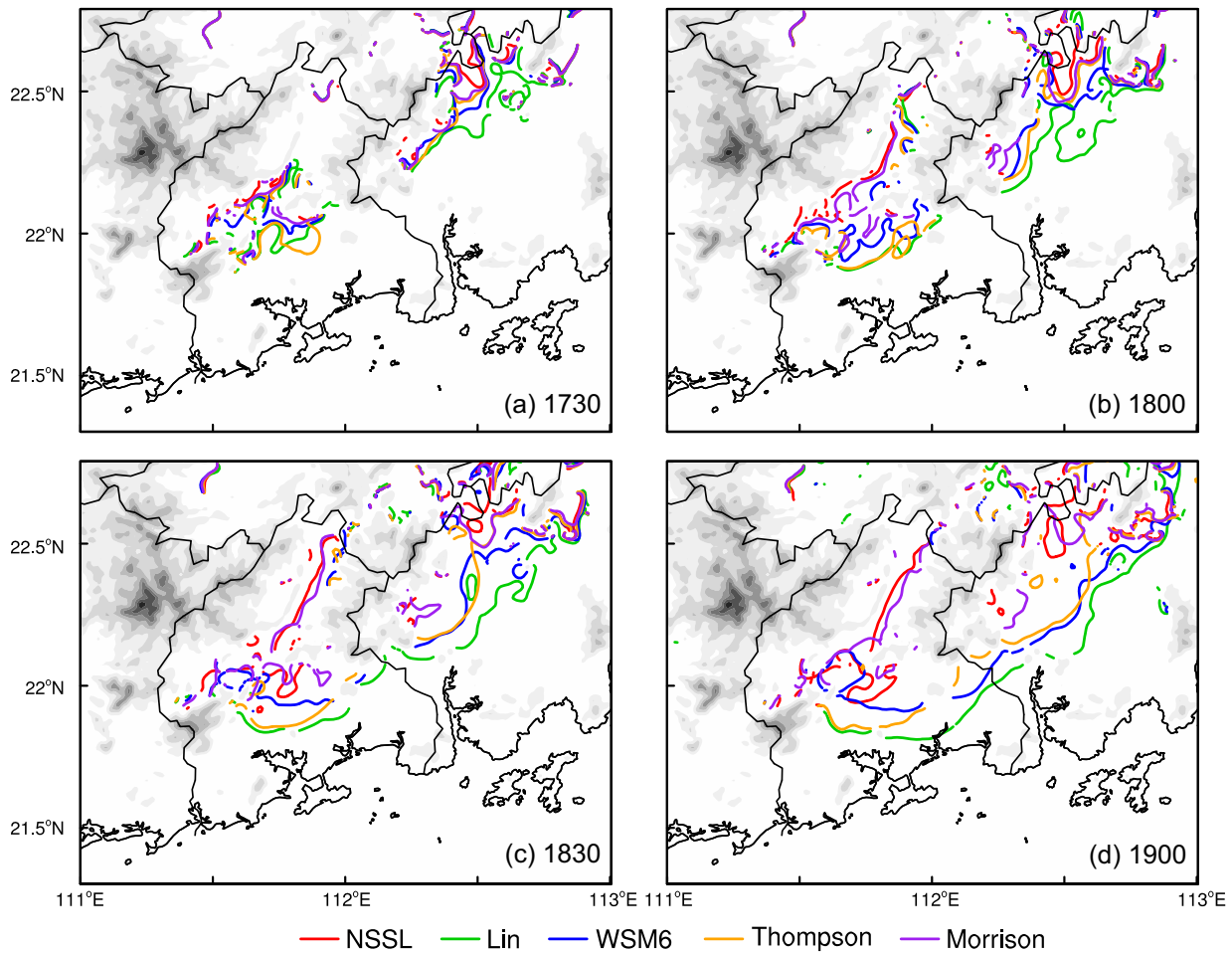
FIGURE 11   Isotherms of 300 K at 100 m above mean sea level from the NSSL simulation (red) and the replacement experiments with the Lin (green), WSM6 (blue), Thompson (orange), and Morrison (purple) schemes at (a) 1730, (b) 1800, (c) 1830, and (d) 1900 UTC June 21, 2017. [Colour figure can be viewed at wileyonlinelibrary.com]

When the mean drop radius (r_0) is larger than 0.1 cm, E_c is set to 0, and the NRACR term becomes 0. In the sensitivity experiment based on the original NSSL simulation, the radius threshold of 0.1 cm is changed to 0.05 cm (NSSL_B). Specifically, in the experiment NSSL_B, E_c and the NRACR term is 0 when r_0 is greater than 0.05 cm.

In the Thompson scheme, the rain self-collection and breakup processes follow Verlinde and Cotton (1993) with some modifications,

$$\text{NRACR} = aEN_rq_r, \qquad (6)$$

where a is the weighting factor, E is the collection efficiency parameter, and q_r is the rainwater mixing ratio. The collection efficiency parameter E is a function of the mean drop size,

$$E = 1 - \exp\left[2,300(D - D_b)\right], \qquad (7)$$

where D_b is the cutoff diameter from which the collection efficiency begins to decrease due to the activated breakup

process. In version 3.9.1 of the WRF model, the Thompson scheme sets D_b to 1.95 mm. In our sensitivity experiment based on the original Thompson simulation, D_b is changed to 2.5 mm according to the observation (i.e., the breakup process becomes less efficient) to test the sensitivity of breakup process (Thompson_B).

Figure 15 shows that after the modification, the simulated DSDs of both schemes fit the observation better. The peaks shift to ~2.5 mm for both schemes. However, both schemes still underestimate smaller raindrops (<1.3 mm) and overestimate larger raindrops (>3.7 mm). In the NSSL_B experiment, the heavy rainfall (> 250 mm) over the middle of Yangjiang and Mt. Tianlu can still be simulated, but the location of heavy rainfall over Yangjiang shifts slightly southward, and the coverage of heavy rainfall near Mt. Tianlu becomes smaller (Figure S1a) compared with the original NSSL simulation (Figure 1b). The cold pools get stronger and spread southward faster (not shown), which partly accounts for the southward shift of the heavy rainfall over Yangjiang. The frequency maxima
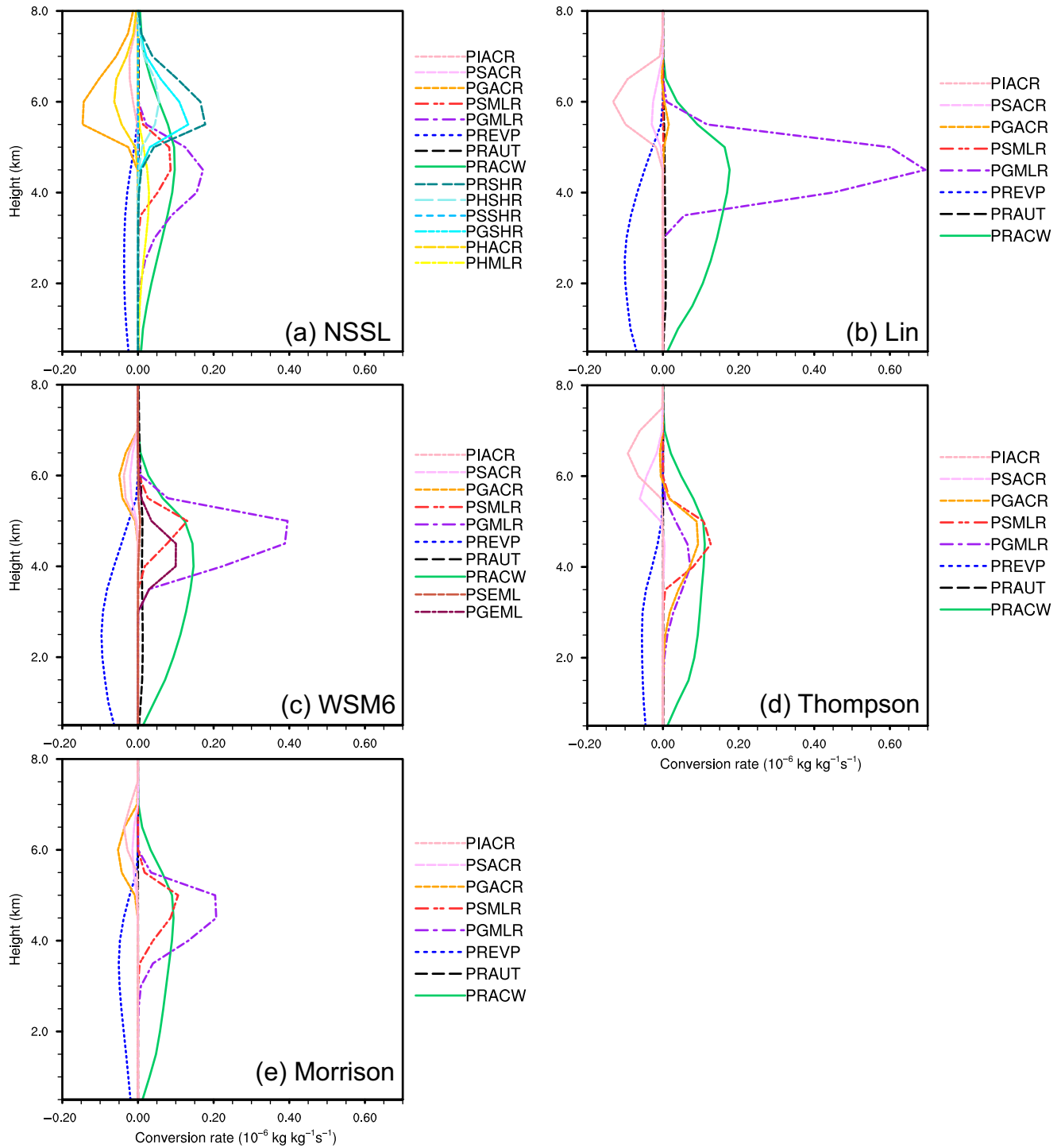
FIGURE 12 As in Figure 8, but for the replacement experiments averaged over the main precipitation region during 1710–0000 UTC June 21–22, 2017. [Colour figure can be viewed at wileyonlinelibrary.com]

of Z_H and Z_{DR} at the low levels in the NSSL_B experiment shift to smaller values (45–50 dBZ and 3 dB, Figure S2) compared with the original NSSL simulation (Figures 5b and 6b), indicating the prevalence of smaller raindrops after modification. In the Thompson_B experiment, the coverage of heavy rainfall over Yangjiang becomes larger, but the accumulated precipitation near Mt. Tianlu

is still less than 200 mm albeit with larger coverage of precipitation over 70 mm (Figure S1b) compared with the original Thompson simulation (Figure 1e). This implies that surface precipitation is a result of many complicated processes and their interaction. Nevertheless, these sensitivity experiments confirm that the rain self-collection and breakup processes greatly affect the simulated rain DSDs.
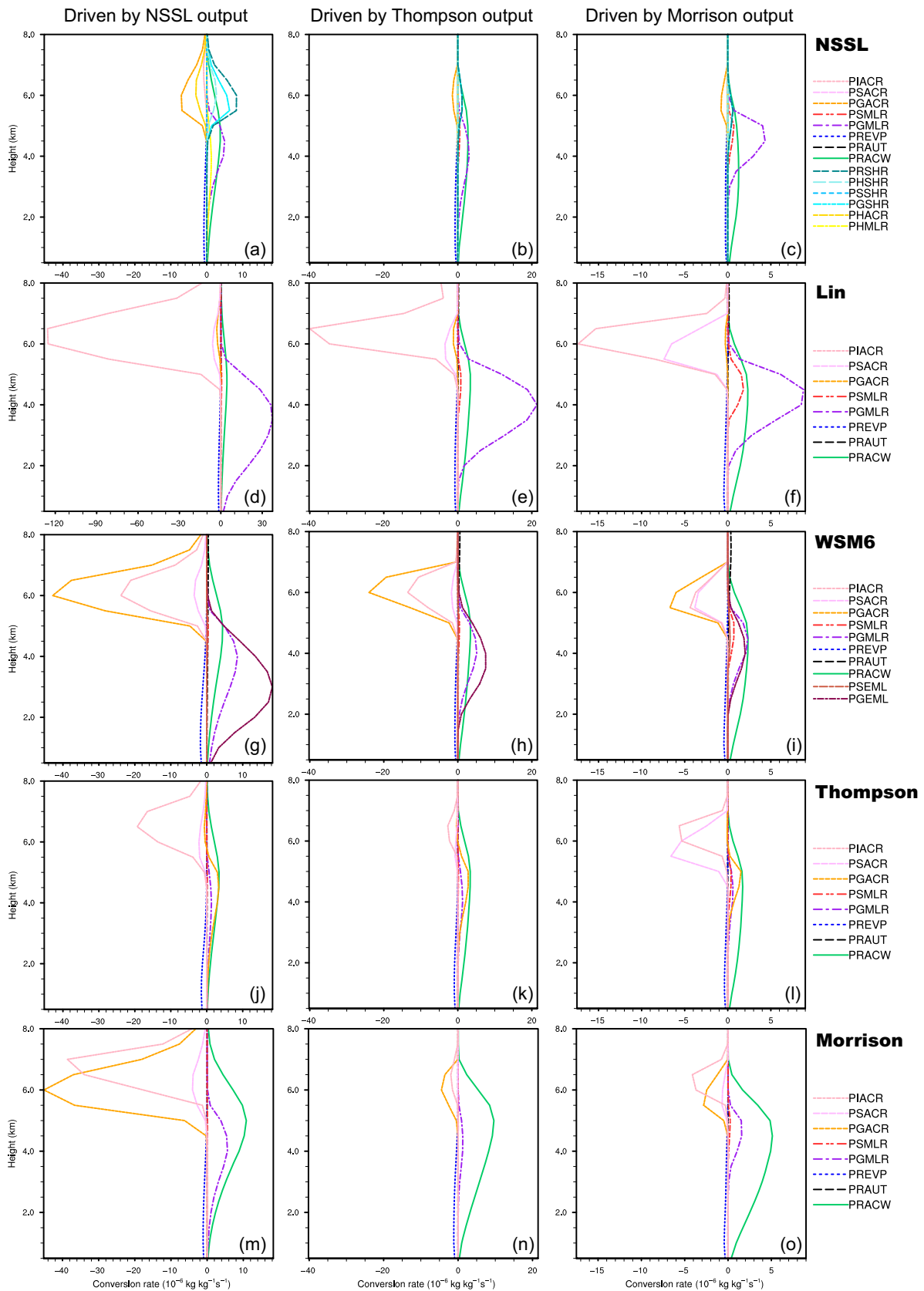
FIGURE 13 As in Figure 12, but are the average results of calculations with the (a–c) NSSL, (d–f) Lin, (g–i) WSM6, (j–l) Thompson, and (m–o) Morrison schemes using identical instantaneous input fields: Left column: the results driven by the output from the NSSL simulation; middle column: the results driven by the output from the Thompson simulation; right column: the results driven by the output from the Morrison simulation. [Colour figure can be viewed at wileyonlinelibrary.com]
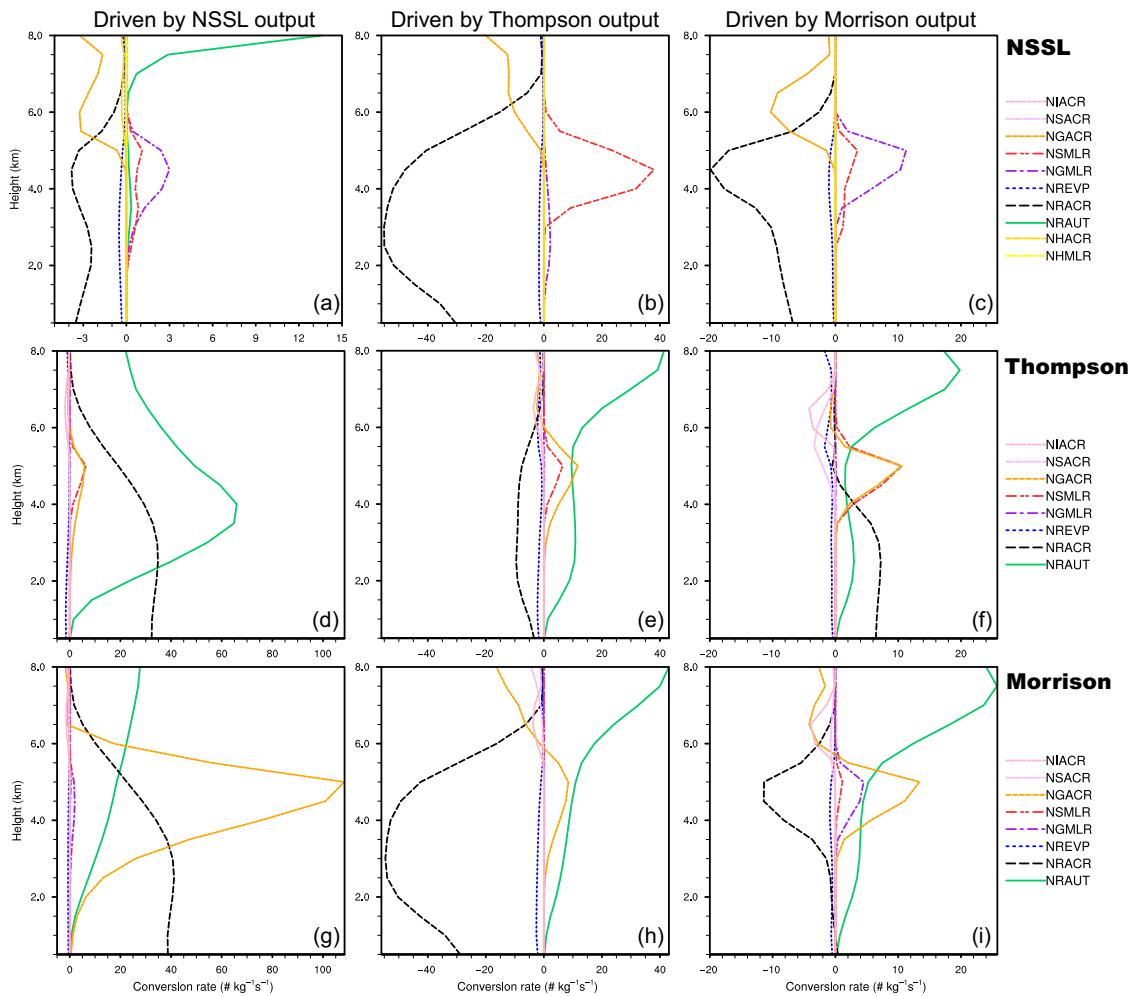
FIGURE 14 As in Figure 9, but are the average results of calculations with the (a–c) NSSL, (d–f) Thompson, and (g–i) Morrison schemes using identical instantaneous input fields: Left column: the results driven by the output from the NSSL simulation; middle column: the results driven by the output from the Thompson simulation; right column: the results driven by the output from the Morrison simulation. [Colour figure can be viewed at wileyonlinelibrary.com]
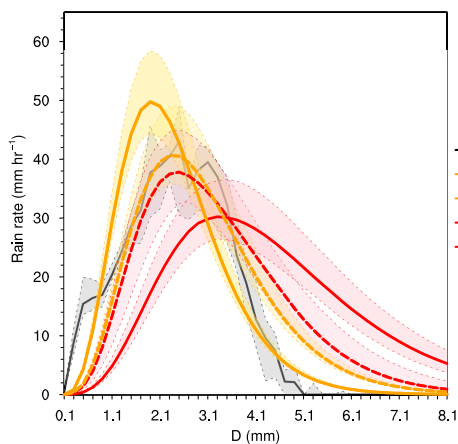
FIGURE 15 As in Figure 3c, but for the original NSSL (solid red line), Thompson (solid orange line) simulations and the sensitivity experiments with modified NSSL (NSSL_B, dashed red line) and Thompson (Thompson_B, dashed orange line) schemes. [Colour figure can be viewed at wileyonlinelibrary.com]

3.6 | Results from two additional extreme rainfall cases

To further consolidate the above conclusions, the five microphysics schemes are used to simulate two more extreme rainfall cases with hourly rainfall exceeding $100\,\text{mm}\cdot\text{hr}^{-1}$. The accumulated rainfall in these two cases is shown in Figures 16 and 17, respectively. One extreme rainfall case is over the coastal region of eastern Guangdong (Huizhou and Shanwei) during June 7–8, 2020 with a maximum hourly rainfall of 136.7 mm (Figure 16a). Convective storms were continuously developed near the coastline due to frictional convergence along the coastline under the influence of a low-level jet. The other extreme rainfall case is over the north of Huizhou on May 31, 2021 with a maximum hourly rainfall of 156.4 mm and a three-hour accumulated rainfall of 400.9 mm (new three-hour record in Guangdong) (Figure 17a). In this
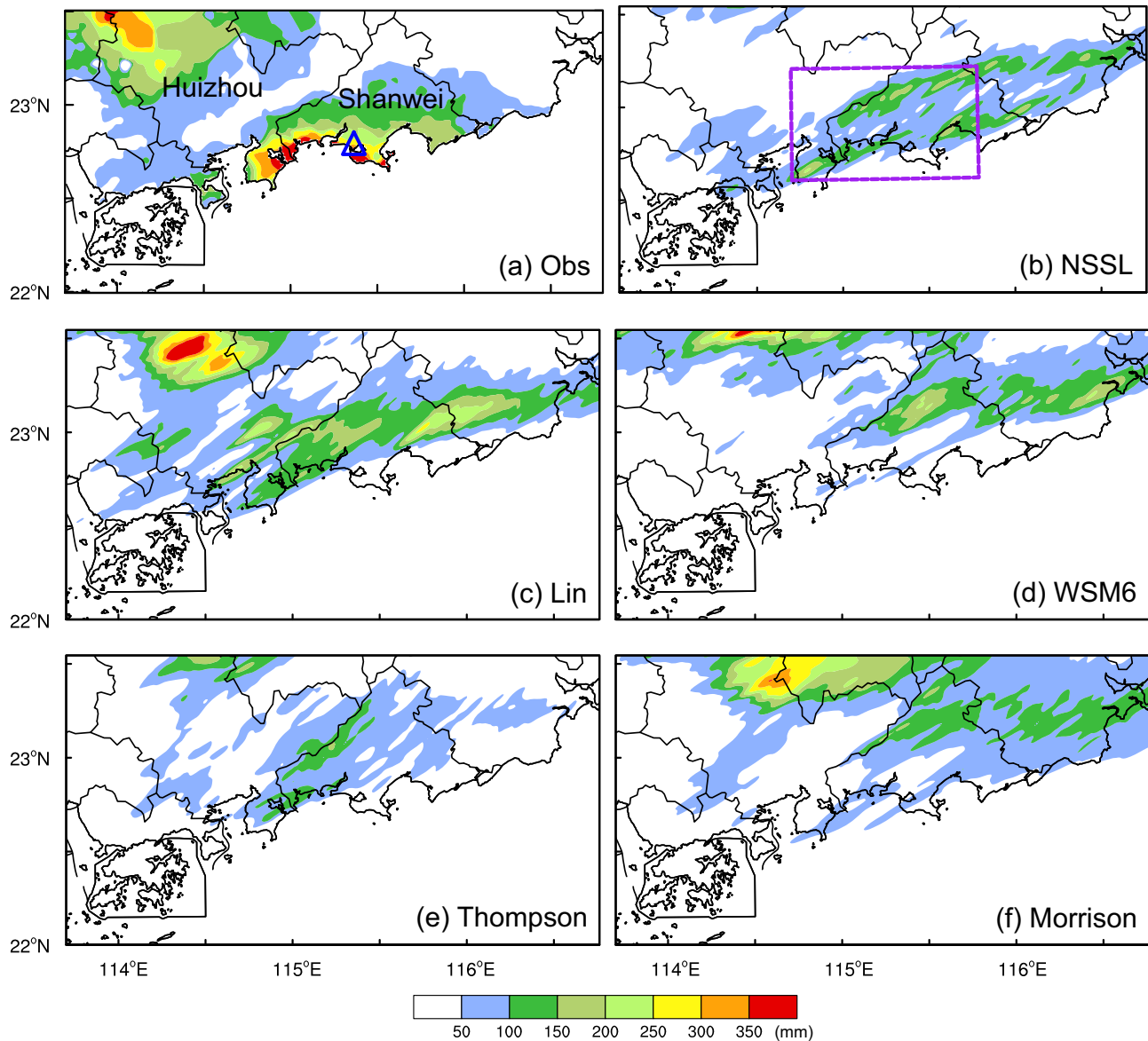
FIGURE 16 The 24-hour (1200 UTC June 7–1200 UTC June 8, 2020) accumulated rainfall (shaded, mm) for the (a) observation, and the simulations with the (b) NSSL, (c) Lin, (d) WSM6, (e) Thompson, and (f) Morrison schemes. The triangle in (a) represents the location of the disdrometer in Shanwei. The rectangle in (b) indicates the area for the statistics of simulated rain DSDs in Figure 18a. [Colour figure can be viewed at wileyonlinelibrary.com]

case, convective storms initiated to the west of Huizhou moved eastward and strongly developed near the mountains in the north of Huizhou.

For the case during June 7–8, 2020 (Figure 16), the Lin and NSSL simulations (Figure 16b,c) outperform other simulations in the generation of heavy rainfall over the coastal region although the accumulated rainfall is weaker than the observation (Figure 16a). Heavy rainfall centers in the WSM6 and Morrison simulations (Figure 16d,f) have a northward displacement compared with the observation. Observation of the disdrometer in Shanwei shows that the rain rate exceeding 100 mm·hr^{-1} is mainly contributed by raindrops with 1.5–4.5-mm diameter (black in Figure 18a).

The simulations using single-moment schemes (green and blue in Figure 18a) have similar diameter of peak rain rate to the observation (∼2.5 mm) but they overpredict raindrops smaller than 2 mm and underpredict raindrops with 3–4.5-mm diameter. The diameter of peak rain rate is larger in the NSSL simulation (∼4 mm, red in Figure 18a) than the observation while those in the Thompson and Morrison simulations (orange and purple in Figure 18a) are smaller (∼2 mm). The overprediction of large (small) raindrops is distinct in the NSSL (Thompson) simulation (Figure 18a).

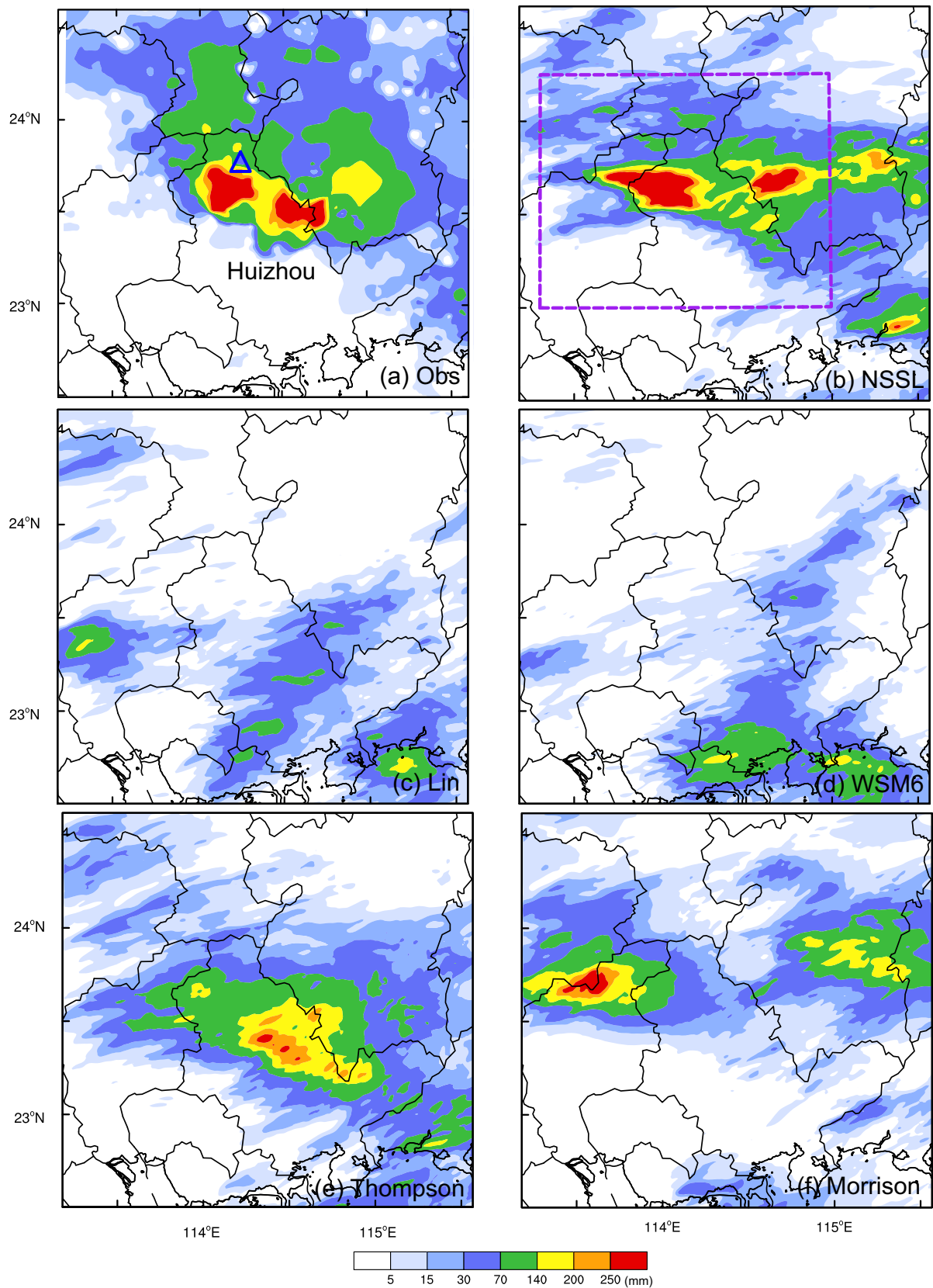For the case on May 31, 2021 (Figure 17), the NSSL simulation (Figure 17b) performs the best in terms of the

FIGURE 17 The 10-hour (1600 UTC May 30–0200 UTC May 31, 2021) accumulated rainfall (shaded, mm) for the (a) observation, and the simulations with the (b) NSSL, (c) Lin, (d) WSM6, (e) Thompson, and (f) Morrison schemes. The triangle in (a) represents the location of the disdrometer in Huizhou. The rectangle in (b) indicates the area for the statistics of simulated rain DSDs in Figure 18b. [Colour figure can be viewed at wileyonlinelibrary.com]
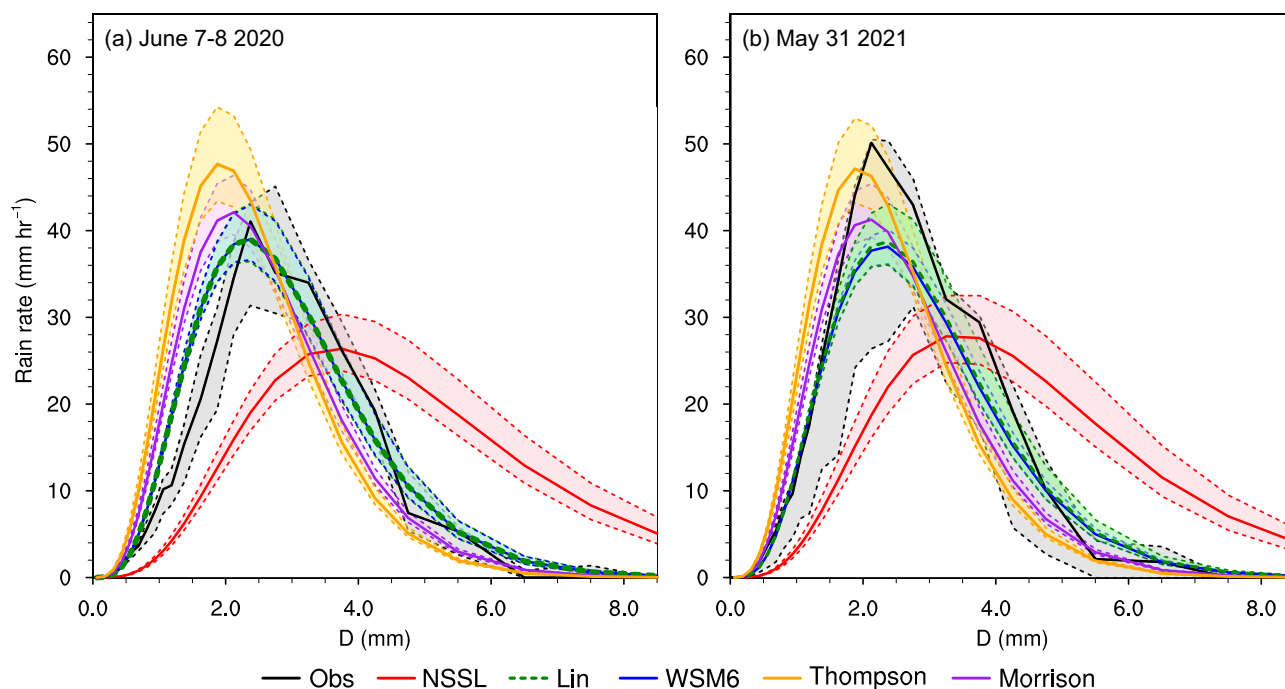
FIGURE 18   As in Figure 3, but for observed and simulated distribution of rain rate for the cases (a) during June 7–8, 2020, and (b) on May 31, 2021. Only the distribution data with integral precipitation intensity $R \geq 100 \, \text{mm·hr}^{-1}$ are shown.

intensity and location of heavy rainfall over the north of Huizhou. The Thompson simulation (Figure 17e) produces heavy rainfall in Huizhou but with weaker intensity and southward displacement error. The other simulations miss the heavy rainfall in Huizhou. Observation of the disdrometer in the north of Huizhou shows that raindrops with 1–4 mm diameter make a major contribution to heavy rainfall with a peak value at approximately 2 mm (black in Figure 18b). Compared with the observation, the NSSL scheme produces evidently more large raindrops (>4 mm) (red in Figure 18b). The drop diameter of peak rain rate in the NSSL simulation (3–3.5 mm) is larger than that in the observation while that in the Thompson simulation (~1.8 mm, orange in Figure 18b) is smaller, which is consistent with the analysis for the June 21–22, 2017 case. The simulations of these two additional cases suggest the possible general issue for the NSSL scheme to simulate the extreme rainfall over South China, in which simulated extreme rainfall rate is not from the right representation of rain drop size distribution.

4 | SUMMARY AND CONCLUSIONS

In this study, a detailed process-based evaluation of five bulk microphysics schemes (including two single-moment schemes and three double-moment schemes) in the simulation of an extreme rainfall event occurring under weak synoptic lifting over the mountainous coast of South

China is first performed using the observations from the polarimetric radar and two-dimensional video disdrometer. Major findings are summarized as follows.

All the schemes produce the heavy rainfall over the middle of Yangjiang and the NSSL scheme also simulates the heavy rainfall over Mt. Tianlu well, but other schemes underestimate the rainfall over Mt. Tianlu. However, the "right" precipitation pattern is not produced by accurate microphysical properties as observed. Observational analysis shows that large amounts of small- and medium-sized (1–4 mm) raindrops are the main contributors to the heavy rainfall. However, all the simulations do not accurately replicate the observed DSD, and tend to underpredict the medium-sized raindrops.

Notable differences are found in the simulated rain drop size distribution among these microphysics schemes. The Lin, WSM6, and Morrison simulations show better agreement with the observed DSD in the small-sized range (1–2 mm) for higher rain rates while the Thompson simulation produces more small-sized raindrops. The NSSL simulation exhibits a broad distribution with more large raindrops than other simulations, which is related to its more efficient rain self-collection process at the low levels. The NSSL simulation is able to produce high rain rates close to the observation, but overestimates the low-level Z_H and Z_{DR}. The above DSD features in these schemes are also seen in the simulations of two other extreme rainfall cases, implying the possible deficiency in these schemes for simulating extreme rainfall over South China.

The efficient collection of rain/cloud water by rain and a proper rain evaporation rate play a leading role in the formation of extreme rainfall in the NSSL simulation. Proper interaction between environmental flows and cold-pool outflows associated with rain evaporation is one of the key factors in the simulation of convective systems over South China with a moist environment (e.g., Qian *et al.*, 2018; Huang *et al.*, 2019a; Huang *et al.*, 2019b; Huang *et al.*, 2020). Modification of the rain self-collection/breakup processes in the microphysics schemes based on the observation shows promising improvement in the simulated rain DSDs.

In a nutshell, there were two main aspects which account for the "right" rainfall result but not from the "right" representation of rain microphysics, particular in the NSSL simulation. On the one hand, the NSSL simulation has a broad rain DSD with overpredicted large raindrops and thus produces a high rain intensity. On the other hand, the representation of rain DSD is also related to rain evaporation in the microphysics scheme. It should be noted that there are lots of uncertainties or biases in models, not only in physics schemes but also in environmental conditions such as wind flows and humidity. The NSSL simulation produces cold pools associated with rain evaporation interacting with environmental flows that can maintain the convective system and then affect the duration of heavy rainfall. The rain intensity and duration are just in place to produce "right" accumulated precipitation in the cases presented in this study.

This study indicates that microphysical characteristics should be carefully examined in addition to surface precipitation when simulating extreme rainfall. In particular, when discussing some factors strongly related to microphysical processes such as cold pools, it is beneficial to examine more microphysics schemes other than draw a conclusion from only one microphysics scheme (Li *et al.*, 2015; Mallinson and Lasher-Trapp, 2019; Marion and Trapp, 2019). In the future, more efforts are needed to improve the representation of rain self-collection/breakup and evaporation processes for the extreme rainfall over South China based on more observations (especially observations at different height levels) of more cases. The impact of improved DSD on rainfall forecasts also deserves further study with process-based evaluations of more cases. Moreover, the number concentration of cloud condensation nuclei has an effect on the rain self-collection and evaporation processes (Warner, 1968; Xue and Feingold, 2006; Rosenfeld *et al.*, 2008; Tao *et al.*, 2012). It is significant to explore how the characteristics of the cloud condensation nuclei over such a mountainous coastal region influence those microphysical processes and the formation of heavy rainfall. Last but not least, uncertainties of ice-phase processes and their roles in storm dynamics and precipitation (Morrison *et al.*, 2020; Huang *et al.*, 2021, 2022; Qu *et al.*, 2022) need to be examined as well.

AUTHOR CONTRIBUTIONS

Huiqi Li: Conceptualization; data curation; formal analysis; funding acquisition; methodology; software; visualization; writing – original draft. **Yongjie Huang:** Conceptualization; formal analysis; methodology; software; writing – review and editing. **Yali Luo:** Funding acquisition; supervision; writing – review and editing. **Hui Xiao:** Data curation; software; writing – review and editing. **Ming Xue:** Methodology; writing – review and editing. **Xiantong Liu:** Data curation. **Lu Feng:** Data curation.

ACKNOWLEDGEMENTS

CONFLICT OF INTEREST

The authors declare no conflicts of interest.

DATA AVAILABILITY STATEMENT

The ERA-Interim data are available from https://apps.ecmwf.int/datasets/data/interim-full-daily/. The data in this study have been archived at the Harvard data server (https://doi.org/10.7910/DVN/SFC8EQ). Version 3.9.1 of the WRF model can be downloaded from https://www2.mmm.ucar.edu/wrf/users/download/get_sources.html.

ORCID

Huiqi Li https://orcid.org/0000-0001-6151-955X
Yongjie Huang https://orcid.org/0000-0001-7883-8768
Yali Luo https://orcid.org/0000-0002-5447-3255
Hui Xiao https://orcid.org/0000-0003-2929-0323
Ming Xue https://orcid.org/0000-0003-1976-3238
Xiantong Liu https://orcid.org/0000-0001-5110-7359

REFERENCES

Barnes, H.C. and Houze, R.A., Jr. (2016) Comparison of observed and simulated spatial patterns of ice microphysical processes in tropical oceanic mesoscale convective systems. *Journal of Geophysical Research: Atmospheres*, 121, 8269–8296. https://doi.org/10.1002/2016JD025074.

Benjamin, S.G., Grell, G.A., Brown, J.M., Smirnova, T.G. and Bleck, R. (2004) Mesoscale weather prediction with the RUC hybrid isentropic-terrain-following coordinate model. *Monthly Weather Review*, 132, 473–494. https://doi.org/10.1175/1520-0493(2004)132<0473:MWPWTR>2.0.CO;2.

Bougeault, P., Binder, P., Buzzi, A., Dirks, R., Houze, R., Kuettner, J., et al. (2001) The MAP special observing period. *Bulletin of the American Meteorological Society*, 82, 433–462. https://doi.org/10.1175/1520-0477(2001)082<0433:TMSOP>2.3.CO;2.

Brandes, E.A., Zhang, G. and Vivekanandan, J. (2002) Experiments in rainfall estimation with a polarimetric radar in a subtropical environment. *Journal of Applied Meteorology and Climatology*, 41, 674–685. https://doi.org/10.1175/1520-0450(2002)041<0674:EIREWA>2.0.CO;2.

Brandes, E.A., Zhang, G. and Vivekanandan, J. (2004) Drop size distribution retrieval with polarimetric radar: model and application. *Journal of Applied Meteorology*, 43, 461–475. https://doi.org/10.1175/1520-0450(2004)043<0461:DSDRWP>2.0.CO;2.

Brown, B.R., Bell, M.M. and Frambach, A.J. (2016) Validation of simulated hurricane drop size distributions using polarimetric radar. *Geophysical Research Letters*, 43, 910–917. https://doi.org/10.1002/2015GL067278.

Bryan, G.H. and Morrison, H. (2012) Sensitivity of a simulated squall line to horizontal resolution and parameterization of microphysics. *Monthly Weather Review*, 140, 202–5115. https://doi.org/10.1175/MWR-D-11-00046.1.

Conrick, R. and Mass, C.F. (2019) An evaluation of simulated precipitation characteristics during OLYMPEX. *Journal of Hydrometeorology*, 20, 1147–1164. https://doi.org/10.1175/JHM-D-18.0144.1.

Dawson, D.T., Xue, M., Milbrandt, J.A. and Yau, M.K. (2010) Comparison of evaporation and cold pool development between single-moment and multimoment bulk microphysics schemes in idealized simulations of tornadic thunderstorms. *Monthly Weather Review*, 138, 1152–1171. https://doi.org/10.1175/2009MWR2956.1.

Dee, D.P., Uppala, S.M., Simmons, A.J., Berrisford, P., Poli, P., Kobayashi, S., Andrae, U., Balmaseda, M.A., Balsamo, G., Bauer, P., Bechtold, P., Beljaars, A.C.M., van de Berg, L., Bidlot, J., Bormann, N., Delsol, C., Dragani, R., Fuentes, M., Geer, A.J., Haimberger, L., Healy, S.B., Hersbach, H., Hólm, E.V., Isaksen, L., Kållberg, P., Köhler, M., Matricardi, M., McNally, A.P., Monge-Sanz, B.M., Morcrette, J.J., Park, B.K., Peubey, C., de Rosnay, P., Tavolato, C., Thépaut, J.N. and Vitart, F. (2011) The ERA-Interim reanalysis: configuration and performance of the data assimilation system. *Quarterly Journal of the Royal Meteorological Society*, 137, 553–597. https://doi.org/10.1002/qj.828.

Dong, X. and Li, J. (2023) Simulations of an extreme rainstorm event (1056.7 mm/day) along the South China coast: cloud microphysical processes and maintenance mechanism of rainstorm. *Atmospheric Research*, 282, 106541. https://doi.org/10.1016/j.atmosres.2022.106541.

Furtado, K., Field, P.R., Luo, Y., Liu, X., Guo, Z., Zhou, T., Shipway, B.J., Hill, A.A. and Wilkinson, J.M. (2018) Cloud microphysical factors affecting simulations of deep convection during the presummer rainy season in southern China. *Journal of Geophysical Research: Atmospheres*, 123, 10477–10505. https://doi.org/10.1029/2017JD028192.

Gao, W., Liu, L., Li, J. and Lu, C. (2018) The microphysical properties of convective precipitation over the Tibetan plateau by a subkilometer resolution cloud-resolving simulation. *Journal of Geophysical Research: Atmospheres*, 123, 3212–3227. https://doi.org/10.1002/2017JD027812.

Gao, W., Sui, C.H., Wang, T.C.C. and Chang, W.Y. (2011) An evaluation and improvement of microphysical parameterization from a two-moment cloud microphysics scheme and the southwest monsoon experiment (SoWMEX)/terrain-influenced monsoon rainfall experiment (TiMREX) observations. *Journal of Geophysical Research: Atmospheres*, 116, D19101. https://doi.org/10.1029/2011JD015718.

Grasso, L., Lindsey, D.T., Lim, K.S.S., Clark, A., Bikos, D. and Dembek, S.R. (2014) Evaluation of and suggested improvements to the WSM6 microphysics in WRF-ARW using synthetic and observed GOES-13 imagery. *Monthly Weather Review*, 142, 3635–3650. https://doi.org/10.1175/MWR-D-14-00005.1.

Grell, G.A. and Freitas, S.R. (2014) A scale and aerosol aware stochastic convective parameterization for weather and air quality modeling. *Atmospheric Chemistry and Physics*, 14, 5233–5260. https://doi.org/10.5194/acp-21-6919-2021.

Hong, S.Y. and Lim, J.O.J. (2006) The WRF single-moment 6-class microphysics schemes (WSM6). *Journal of the Korean Meteorological Society*, 42, 129–151.

Hong, S.Y., Noh, Y. and Dudhia, J. (2006) A new vertical diffusion package with an explicit treatment of entrainment processes. *Monthly Weather Review*, 134, 2318–2341. https://doi.org/10.1175/MWR3199.1.

Houze, R.A., Jr., McMurdie, L.A., Petersen, W.A., Schwaller, M.R., Baccus, W., Lundquist, J.D., Mass, C.F., Nijssen, B., Rutledge, S.A., Hudak, D.R., Tanelli, S., Mace, G.G., Poellot, M.R., Lettenmaier, D.P., Zagrodnik, J.P., Rowe, A.K., DeHart, J.C., Madaus, L.E., Barnes, H.C. and Chandrasekar, V. (2017) The Olympic Mountains experiment (OLYMPEX). *Bulletin of the American Meteorological Society*, 98, 2167–2188. https://doi.org/10.1175/BAMS-D-16-0182.1.

Huang, Y., Liu, Y., Liu, Y. and Knievel, J. (2019a) Budget analyses of a record-breaking rainfall event in the coastal metropolitan city of Guangzhou, China. *Journal of Geophysical Research-Atmospheres*, 124, 9391–9406. https://doi.org/10.1029/2018JD030229.

Huang, Y., Liu, Y., Liu, Y., Li, H. and Knievel, J. (2019b) Mechanisms for a record-breaking rainfall in the coastal metropolitan city of Guangzhou, China: observation analysis and nested very-large-eddy simulation with the WRF model. *Journal of Geophysical Research-Atmospheres*, 124, 1370–1391. https://doi.org/10.1029/2018JD029668.

Huang, Y., Wang, Y., Xue, L., Wei, X., Zhang, L. and Li, H. (2020) Comparison of three microphysics parameterization schemes in the WRF model for an extreme rainfall event in the coastal metropolitan city of Guangzhou, China. *Atmospheric Research*, 240, 104939. https://doi.org/10.1016/j.atmosres.2020.104939.

Huang, Y., Wu, W., McFarquhar, G.M., Wang, X., Morrison, H., Ryzhkov, A., Hu, Y., Wolde, M., Nguyen, C., Schwarzenboeck, A., Milbrandt, J., Korolev, A.V. and Heckman, I. (2021) Microphysical processes producing high ice water contents (HIWCs) in tropical convective clouds during the HAIC-HIWC field campaign: evaluation of simulations using bulk microphysical schemes. *Atmospheric Chemistry and Physics*, 21, 6919–6944. https://doi.org/10.5194/acp-21-6919-2021.

Huang, Y., Wu, W., McFarquhar, G.M., Xue, M., Morrison, H., Milbrandt, J., Korolev, A.V., Hu, Y., Qu, Z., Wolde, M., Nguyen, C., Schwarzenboeck, A. and Heckman, I. (2022) Microphysical processes producing high ice water contents (HIWCs) in tropical convective clouds during the HAIC-HIWC field campaign:

dominant role of secondary ice production. *Atmospheric Chemistry and Physics*, 22, 2365–2384. https://doi.org/10.5194/acp-22-2365-2022.

Iacono, M.J., Delamere, J.S., Mlawer, E.J., Shephard, M.W., Cough, S.A. and Collins, W.D. (2008) Radiative forcing by long-lived greenhouse gases: calculations with the AER radiative transfer models. *Journal of Geophysical Research*, 113, D13103. https://doi.org/10.1029/2008JD009944.

Igel, A.L., Igel, M.R. and van den Heever, S.C. (2015) Make it a double? Sobering results from simulations using single-moment microphysics schemes. *Journal of the Atmospheric Sciences*, 72, 910–925. https://doi.org/10.1175/JAS-D-14-0107.1.

Johnson, M., Jung, Y., Dawson, D.T. and Xue, M. (2016) Comparison of simulated polarimetric signatures in idealized supercell storms using two-moment bulk microphysics schemes in WRF. *Monthly Weather Review*, 144, 971–996. https://doi.org/10.1175/MWR-D-15-0233.1.

Jung, Y., Xue, M. and Zhang, G. (2010) Simulations of polarimetric radar signatures of a supercell storm using a two-moment bulk microphysics scheme. *Journal of Applied Meteorology and Climatology*, 49, 146–163. https://doi.org/10.1175/2009JAMC2178.1.

Jung, Y., Zhang, G. and Xue, M. (2008) Assimilation of simulated polarimetric radar data for a convective storm using ensemble Kalman filter. Part I: observation operators for reflectivity and polarimetric variables. *Monthly Weather Review*, 136, 2228–2245. https://doi.org/10.1175/2007MWR2083.1.

Kessler, E. (1995) On the continuity and distribution of water substance in atmospheric circulations. *Atmospheric Research*, 38(1–4), 109–145. https://doi.org/10.1016/0169-8095(94)00090-Z.

Kumjian, M.R. (2013) Principles and applications of dual-polarization weather radar. Part I: description of the polarimetric radar variables. *Journal of Operational Meteorology*, 1, 226–242. https://doi.org/10.15191/nwajom.2013.0119.

Li, H., Huang, Y., Hu, S., Wu, N., Liu, X. and Xiao, H. (2021) Roles of terrain, surface roughness, and cold pool outflows in an extreme rainfall even over the coastal region of South China. *Journal of Geophysical Research: Atmospheres*, 126, e2021JD035556. https://doi.org/10.1029/2021JD035556.

Li, Z., Zuidema, P., Zhu, P. and Morrison, H. (2015) The sensitivity of simulated shallow cumulus convection and cold pools to microphysics. *Journal of the Atmospheric Sciences*, 72, 3340–3355. https://doi.org/10.1175/JAS-D-14-0099.1.

Lin, Y. and Colle, B.A. (2009) The 4-5 December 2001 IMPROVE-2 event: observed microphysics and comparisons with the weather research and forecasting model. *Monthly Weather Review*, 137, 1372–1392. https://doi.org/10.1175/2008MWR2653.1.

Lin, Y.L., Farley, R.D. and Orville, H.D. (1983) Bulk parameterization of the snow field in a cloud model. *Journal of Applied Meteorology and Climatology*, 22(6), 1065–1092. https://doi.org/10.1175/1520-0450(1983)022<1065:BPOTSF>2.0.CO;2.

Luo, L., Xue, M., Zhu, K. and Zhou, B. (2018) Explicit prediction of hail in a long-lasting multi-cellular convective system in eastern China using multi-moment microphysics schemes. *Journal of the Atmospheric Sciences*, 72, 3115–3137. https://doi.org/10.1175/JAS-D-17-0302.1.

Luo, Y., Wang, Y., Wang, H., Zheng, Y. and Morrison, H. (2010) Modeling convective-stratiform precipitation processes on a Mei-Yu front with the weather research and forecasting model: comparison with observations and sensitivity to cloud microphysics parameterizations. *Journal of Geophysical Research: Atmospheres*, 115, D18117. https://doi.org/10.1029/2010JD013873.

Luo, Y., Wu, M., Ren, F., Li, J. and Wong, W.K. (2016) Synoptic situations of extreme hourly precipitation over China. *Journal of Climate*, 29, 8703–8719. https://doi.org/10.1175/JCLI-D-16-0057.1.

Luo, Y., Xu, K.M., Morrison, H. and McFarquhar, G. (2008) Arctic mixed-phase clouds simulated by a cloud-resolving model: comparison with ARM observations and sensitivity to microphysics parameterizations. *Journal of the Atmospheric Sciences*, 65, 1285–1303. https://doi.org/10.1175/2007JAS2467.1.

Luo, Y., Zhang, R., Wan, Q., Wang, B., Wong, W.K., Hu, Z., et al. (2017) The southern China monsoon rainfall experiment (SCMREX). *Bulletin of the American Meteorological Society*, 98, 999–1013. https://doi.org/10.1175/JCLI-D-16-0057.1.

Mallinson, H.M. and Lasher-Trapp, S.G. (2019) An investigation of hydrometeor latent cooling upon convective cold pool formation, sustainment, and properties. *Monthly Weather Review*, 147, 3205–3222. https://doi.org/10.1175/MWR-D-18-0382.1.

Mansell, E.R., Ziegler, C.L. and Bruning, E.C. (2010) Simulated electrification of a small thunderstorm with two-moment bulk microphysics. *Journal of the Atmospheric Sciences*, 67, 171–194. https://doi.org/10.1175/2009JAS2965.1.

Marion, G.R. and Trapp, R.J. (2019) The dynamical coupling of convective updrafts, downdrafts, and cold pools in simulated supercell thunderstorms. *Journal of Geophysical Research: Atmospheres*, 124, 664–683. https://doi.org/10.1029/2018JD029055.

Milbrandt, J.A. and Yau, M.K. (2005) A multimoment bulk microphysics parameterization. Part I: analysis of the role of the spectral shape parameter. *Journal of the Atmospheric Sciences*, 62(9), 3051–3064. https://doi.org/10.1175/JAS3534.1.

Morrison, H. and Grabowski, W.W. (2007) Comparison of bulk and bin warm rain microphysics models using a kinematic framework. *Journal of the Atmospheric Sciences*, 64, 2839–2861. https://doi.org/10.1175/jas3980.

Morrison, H., Tessendorf, S.A. and Thompson, G. (2012) Sensitivity of a simulated midlatitude squall line to parameterization of raindrop breakup. *Monthly Weather Review*, 140, 2437–2460. https://doi.org/10.1175/mwr-d-11-00283.1.

Morrison, H., Thompson, G. and Tatarskii, V. (2009) Impact of cloud microphysics on the development of trailing stratiform precipitation in a simulated squall line: comparison of one- and two-moment schemes. *Monthly Weather Review*, 137, 991–1007. https://doi.org/10.1175/2008MWR2556.1.

Morrison, H., van Lier-Walqui, M., Fridlind, A.M., Grabowski, W.W., Harrington, J.Y., Hoose, C., Korolev, A., Kumjian, M.R., Milbrandt, J.A., Pawlowska, H., Posselt, D.J., Prat, O.P., Reimel, K.J., Shima, S.I., van Diedenhoven, B. and Xue, L. (2020) Confronting the challenge of modeling cloud and precipitation microphysics. *Journal of Advances in Modeling Earth Systems*, 12, e2019MS001689. https://doi.org/10.1029/2019MS001689.

Naeger, A.R., Colle, B.A. and Molthan, A. (2017) Evaluation of cloud microphysical scheme for a warm frontal snowband during the GPM cold season precipitation experiment (GCPEx). *Monthly Weather Review*, 145, 4627–4650. https://doi.org/10.1175/MWR-D-17-0081.1.

Naeger, A.R., Colle, B.A., Zhou, N. and Molthan, A. (2020) Evaluating warm and cold rain processes in cloud microphysical scheme

using OLYMPEX field measurements. *Monthly Weather Review*, 148, 2163–2190. https://doi.org/10.1175/MWR-D-19-0092.1.

Planche, C., Tridon, F., Banson, S., Thompson, G., Monier, M., Battaglia, A. and Wobrock, W. (2019) On the realism of the rain microphysics representation of a squall line in the WRF model. Part II: sensitivity studies on the rain drop size distributions. *Monthly Weather Review*, 147, 2811–2825. https://doi.org/10.1175/MWR-D-18-0019.1.

Putnam, B.J., Xue, M., Jung, Y., Zhang, G. and Kong, F. (2017) Simulation of polarimetric radar variables from 2013 CAPS spring experiment storm-scale ensemble forecasts and evaluation of microphysics schemes. *Monthly Weather Review*, 145(1), 49–73. https://doi.org/10.1175/mwr-d-15-0415.1.

Qian, Q., Lin, Y., Luo, Y., Zhao, X., Zhao, Z., Luo, Y. and Liu, X. (2018) Sensitivity of a simulated squall line during southern China monsoon rainfall experiment to parameterization of microphysics. *Journal of Geophysical Research: Atmospheres*, 123, 4197–4220. https://doi.org/10.1002/2017JD027734.

Qu, Z., Korolev, A., Milbrandt, J.A., Heckman, I., Huang, Y., McFarquhar, G.M., et al. (2022) The impacts of secondary ice production on microphysics and dynamics in tropical convection. *Atmospheric Chemistry and Physics*, 22, 12287–12310. https://doi.org/10.5194/egusphere-2022-235.

Randall, D.A., Bitz, C.M., Danabasoglu, G., Denning, A.S., Gent, P.R., Gettelman, A., Griffies, S.M., Lynch, P., Morrison, H., Pincus, R. and Thuburn, J. (2018) 100 year of earth system model development. *Meteorological Monographs*, 59, 12.1–12.66. https://doi.org/10.1175/AMSMONOGRAPHS-D-18-0018.1.

Rosenfeld, D., Lohmann, U., Raga, G.B., O'Dowd, C.D., Kulmala, M., Fuzzi, S., Reissell, A. and Andreae, M.O. (2008) Flood or drought: how do aerosols affect precipitation? *Science*, 321, 1309–1313. https://doi.org/10.1126/science.1160606.

Schönhuber, M., Urban, H.E., Poiares Baptista, P.P.V., Randeu, W.L. and Riedler, W. (1997) Weather radar versus 2D-video-disdrometer data. In: Bragg, B., Jr. and Massambani, O. (Eds.) *Weather Radar Technology for Water Resources Management*. Montevideo, Uruguay: Unesco Press, pp. 159–171.

Skamarock, W.C., Klemp, J.B., Dudhia, J., Grill, D.O., Barker, D., Duda, M.G., et al. (2008) *A Description of the Advanced Research WRF Version 3 (No. NCAR/TN-475+STR)*. Boulder, CO: University Corporation for Atmospheric Research. https://doi.org/10.5065/D68S4MVH.

Steiner, M., Houze, R.A. and Yuter, S.E. (1995) Climatological characterization of three-dimensional storm structure from operational radar and rain gauge data. *Journal of Applied Meteorology*, 34(9), 1978–2007. https://doi.org/10.1175/1520-0450(1995)034<1978:ccotds>2.0.co;2.

Stoelinga, M.T., Hobbs, P.V., Mass, C.F., Locatelli, J.D., Colle, B.A., Houze, R.A., Jr., Rangno, A.L., Bond, N.A., Smull, B.F., Rasmussen, R.M., Thompson, G. and Colman, B.R. (2003) Improvement of microphysical parameterization through observational verification experiment. *Bulletin of the American Meteorological Society*, 84, 1807–1826. https://doi.org/10.1175/BAMS-84-12-1807.

Suzuki, K., Stephens, G.L., van den Heever, S.C. and Nakajima, T.Y. (2011) Diagnosis of the warm rain process in cloud-resolving models using joint CloudSat and MODIS observations. *Journal of the Atmospheric Sciences*, 68, 2655–2670. https://doi.org/10.1175/JAS-D-10-05026.1.

Tao, W.K., Chen, J.P., Li, Z., Wang, C. and Zhang, C. (2012) Impact of aerosols on convective clouds and precipitation. *Reviews of Geophysics*, 50, RG2001. https://doi.org/10.1029/2011RG000369.

Tao, W.K. and Moncrieff, M. (2009) Multiscale cloud system modeling. *Reviews of Geophysics*, 47, RG4002. https://doi.org/10.1029/2008RG00276.

Thompson, G., Field, P.R., Rasmussen, R.M. and Hall, W.D. (2008) Explicit forecasts of winter precipitation using an improved bulk microphysics scheme. Part II: implementation of a new snow parameterization. *Monthly Weather Review*, 136, 5095–5115. https://doi.org/10.1175/2008MWR2387.1.

Thompson, G., Rasmussen, R.M. and Manning, K. (2004) Explicit forecasts of winter precipitation using an improved bulk microphysics scheme. Part I: description and sensitivity analysis. *Monthly Weather Review*, 132, 519–542. https://doi.org/10.1175/1520-0493(2004)132<0519:EFOWPU>2.0.CO;2.

Tokay, A., Petersen, W.A., Gatlin, P. and Wingo, M. (2013) Comparison of raindrop size distribution measurements by collocated disdrometers. *Journal of Atmospheric and Oceanic Technology*, 30, 1672–1690. https://doi.org/10.1175/JTECH-D-12-00163.1.

Tridon, F., Planche, C., Mroz, K., Banson, S., Battaglia, A., Baelen, J.V. and Wobrock, W. (2019) On the realism of the rain microphysics representation of a squall line in the WRF model. Part I: evaluation with multifrequency cloud radar doppler spectra observations. *Monthly Weather Review*, 147, 2787–2810. https://doi.org/10.1175/MWR-D-18-0018.1.

Varble, A., Zipser, E.J., Fridlind, A.M., Zhu, P., Ackerman, A.S., Chaboureau, J.P., Fan, J., Hill, A., Shipway, B. and Williams, C. (2014) Evaluation of cloud-resolving and limited area model intercomparison simulations using TWO-ICE observations: 2. Precipitation microphysics. *Journal of Geophysical Research: Atmospheres*, 119, 13919–13945. https://doi.org/10.1002/2013JD021372.

Verlinde, J. and Cotton, W.R. (1993) Fitting microphysical observations of nonsteady convective clouds to a numerical model: an application of the adjoint technique of data assimilation to a kinematic model. *Monthly Weather Review*, 121, 2776–2793. https://doi.org/10.1175/1520-0493(1993)121<2776:FMOONC>2.0.CO;2.

Wang, M., Zhao, K., Pan, Y. and Xue, M. (2020) Evaluation of simulated drop size distributions and microphysical processes using polarimetric radar observations for landfalling typhoon Matmo. *Journal of Geophysical Research: Atmospheres*, 125, e2019JD031527. https://doi.org/10.1029/2019JD031527.

Warner, J. (1968) A reduction in rainfall associated with smoke from sugar-cane fires-an inadvertent weather modification? *Journal of Applied Meteorology and Climatology*, 7, 247–251. https://doi.org/10.1175/1520-0450(1968)007<0247:ARIRAW>2.0.CO;2.

Wu, D., Zhang, F., Chen, X., Ryzhkov, A., Zhao, K., Kumjian, M.R., Chen, X. and Chan, P.W. (2021) Evaluation of microphysics schemes in tropical cyclones using polarimetric radar observations: convective precipitation in an outer rainband. *Monthly Weather Review*, 149, 1055–1068. https://doi.org/10.1175/MWR-D-19-0378.1.

Wu, Z., Zhang, Y., Xie, Y., Zhang, L. and Zheng, H. (2022) Radiance-based assessment of bulk microphysics models with seven hydrometeor species in forecasting super-typhoon Lekima

(2019) near landfall. *Atmospheric Research*, 273, 106173. https://doi.org/10.1016/j.atmosres.2022.106173.

Xue, H. and Feingold, G. (2006) Large-eddy simulations of trade wind cumuli: investigation of aerosol indirect effects. *Journal of the Atmospheric Sciences*, 63, 1605–1622. https://doi.org/10.1175/JAS3706.1.

Yu, M., Miao, S. and Zhang, H. (2018) Uncertainties in the impact of urbanization on heavy rainfall: case study of a rainfall event in Beijing on 7 august 2015. *Journal of Geophysical Research: Atmospheres*, 123, 6005–6021. https://doi.org/10.1029/2018JD028444.

Yu, S., Luo, Y., Wu, C., Zheng, D., Liu, X. and Xu, W. (2022) Convective and microphysical characteristics of extreme precipitation revealed by multisource observations over the Pearl River Delta at monsoon coast. *Geophysical Research Letters*, 49, e2021GL097043. https://doi.org/10.2019/2021GL097043.

Yuter, S.E. and Houze, R.A. (1995) Three-dimensional kinematic and microphysical evolution of florida cumulonimbus. Part II: frequency distributions of vertical velocity, reflectivity, and differential reflectivity. *Monthly Weather Review*, 123(7), 1941–1963. https://doi.org/10.1175/1520-0493(1995)123<1941:tdkame>2.0.co;2.

Zhou, A., Zhao, K., Lee, W.C., Ding, Z., Lu, Y. and Huang, H. (2022) Evaluation and modification of microphysics schemes on the cold pool evolution for a simulated bow echo in Southeast China. *Journal of Geophysical Research: Atmospheres*, 127, e2021JD035262. https://doi.org/10.1029/2021JD035262.

Zhou, Z., Hu, Y., Wang, B., Yin, J., Guo, Y., Kang, Z. and Sun, Y. (2023) Effect of different microphysical parameterizations on the simulations of a South China heavy rainfall. *Journal of Tropical Meteorology*, 29, 68–86. https://doi.org/10.46267/j.1006-8775.2023.006.

Ziegler, C.L. (1985) Retrieval of thermal and microphysical variables in observed convective storms. Part I: model development and preliminary testing. *Journal of the Atmospheric Sciences*, 42(14), 1487–1509. https://doi.org/10.1175/1520-0469(1985)042<1487:ROTAMV>2.0.CO;2.

SUPPORTING INFORMATION

Additional supporting information can be found online in the Supporting Information section at the end of this article.